Effect of surface roughness and industrial heat treatments on the microstructure and mechanical properties of Ti6Al4V alloy manufactured by laser powder bed fusion in different built orientations

Effect of surface roughness and industrial heat treatments on the microstructure and mechanical properties of Ti6Al4V alloy manufactured by laser powder bed fusion in different built orientations

Emanuela Cerri[1], Emanuele Ghio[1,*], Giovanni Bolelli[2, 3, 4]

[1.] Department of Engineering and Architecture, University of Parma, Via G. Usberti 181/A, 43124 – Parma (Italy)

[2.] Department of Engineering "Enzo Ferrari", University of Modena e Reggio Emilia, Via Pietro Vivarelli 10/1, 41125 – Modena (Italy)

[3.] InterMech MO.RE. Centro Interdipartimentale per la Ricerca Applicata e i Servizi nel Settore della Meccanica Avanzata e della Motoristica, Università di Modena e Reggio Emilia, Via Pietro Vivarelli 2, 41125 – Modena (Italy)

[4.] Consorzio Interuniversitario Nazionale per la Scienza e Tecnologia dei Materiali (INSTM), Local Unit: Università di Modena e Reggio Emilia, Via Pietro Vivarelli 10/1, 41125 – Modena (Italy)

*corresponding author. e-mail address: emanuele.ghio@unipr.it

Abstract

The emergence of powder bed fusion in recent years has made it one of the most demanded additive manufacturing technologies for Ti6Al4V alloys in the biomedical and aerospace industries due to its ease of part fabrication with complex geometry. However, Ti6Al4V components require a post-processing treatment to optimize their mechanical properties for engineering applications. The present study offers an analysis of the effects of different industrial heat treatments (704 °C for 120 min, 740 °C for 130 min) on the microstructure and tensile properties of Ti6Al4V samples manufactured by laser powder bed fusion in different orientations (Z, 45°, XY and XZ). These heat treatments were selected to improve the mechanical properties of the as-built material and to obtain samples representative of real industrial applications. SEM observations illustrated that the α' martensite grown in the columnar parent β-grains was converted into an α+β mixture after both heat treatments. EBSD showed that the newly formed α phase maintained, inside the parent β grains, the same orientation relationship as the as-built α' martensite. However, on a macroscopic scale, the α phase exhibited no preferential orientation. The heat-treated samples, which exhibited approximately 10% lower ultimate tensile strength and yield strength than the as built samples but a 10–13% higher elongation, were practically isotropic in their mechanical response. What little anisotropy was left

was mainly attributed to few elongated interlamellar pores. The sandblasting process was also investigated; it did not affect the static mechanical properties of the samples but it reduced the Ra values by 25%. Finally, Vickers microhardness vs. strength relationships were studied by considering the α-phase orientation.

Keywords

Ti6Al4V-ELI alloy; Laser Powder Bed Fusion; mechanical properties; crystallographic texture; hardness.

---

1. Introduction

Laser powder bed fusion (L-PBF) is a technology belonging to the powder bed fusion processes in the field of Additive Manufacturing (AM) [1]. This manufacturing process allows to print 3D metal objects with layer upon layer methodology using a single or multi laser beam [2]; a fully dense part with a homogeneous microstructure can be obtained at the same time [3,4]. Different sample orientations with respect to the build direction on the platform can influence the measured tensile strengths and, therefore, the mechanical behavior of a 3D component can change in relation to its geometry. As reported by Simonelli et al. [5], Ti6Al4V alloy samples manufactured by L-PBF in the horizontal (XZ) direction have higher strength than vertical samples (Z direction).

Ti6Al4V is an α+β titanium alloy which provides an excellent combination of high tensile properties, low density, and high temperature resistance, suitable for different application fields (i.e. aerospace, automotive and biomedical) [6-12]. The presence of both α and β phases at room temperature is made possible by the alloying elements. Aluminium stabilizes the α phase (hcp – hexagonal close packed) whilst vanadium stabilizes the β phase (bcc – body centred cubic). The phase diagram of the Ti-Al-V system shows that the α+β region is separated from the β region by the β-transus at ~ 995°C [6,13]. So, upon solidification, the liquid phase is first transformed into β-grains. During the subsequent cooling, the β phase begins to transform to α phase below the β-transus. During L-PBF process, β-grains grow along the build direction in each layer and Ti6Al4V manufactured via

laser powder bed fusion is typically anisotropic [5,14-16]. This process is characterized by high temperature gradients $\left(\sim 10^6 \frac{K}{m}\right)$ and high cooling rates $\left(10^6 - 10^8 \frac{K}{s}\right)$ that promote the formation of α' martensite within the prior columnar β-grains [17]. The formation of α' martensite causes high tensile strength but low ductility in Ti-6Al-4V produced by laser powder bed fusion. More specifically, the mechanical properties of the as built Ti6Al4V parts depend on the quantity, shape and morphology of α' martensite and the spacing between needles. Notably, different types of α' martensite co-exist in Ti6Al4V due to the complex thermal history of the material. After an element of material is solidified, it typically experiences several further heating and fast cooling cycles as the laser scans nearby locations. In the as-built Ti6Al4V, the yield strength (YS) and the ultimate tensile strength (UTS) are typically greater than 1 GPa, but the elongation is lower than 10% [5,16,17]. Many applications require a different balance between tensile strength and elongation. Therefore, post process heat treatments at temperatures below the β-transus must be considered to satisfy the current standard specification and to maintain the high strength conferred by the AM process.

Heat treatments below the β-transus induce few microstructural changes: α' martensite does not completely transform to α+β, and the columnar prior β-grains remain visible. Heat treatments at about 700 °C produce a microstructure characterized by fine α'/α-phase with acicular morphology. The formation of a greater quantity of α+β phase within the columnar prior β-grains is detected by increasing the temperature close to the β-transus [3,18-20]. If the temperature remains below the β-transus, the time is not decisive for the grain growth because both the α' and β phases tend to coarsen, hindering their respective growths [18,19,21,22]. In this scenario, the Vickers microhardness measurements can confer a first evaluation of the strength reached by the heat-treated samples without the execution of the tensile test. In the discussion section several relationships will be discussed.

The surface roughness of the L-PBF process, which varies from 30 to 70 μm (Ra) [23-25], influences the mechanical properties. Sun et al. [26] showed an increment of ultimate tensile strength (UTS), yield strength (YS) and ductility when Ra is reduced from 39 to 0.13 μm. Jamshidi et al. [9]

showed that sandblasting and chemical etching improved the tensile strengths and ductility of as-built samples. The sandblasting process is quite often performed on Ti6Al4V samples used in the biomedical field to facilitate osteointegration rather than to increase the mechanical properties as will be discussed in the following sections.

The aim of this work is to evaluate the effects of two heat treatments, characterized by different peak temperatures and also different cooling paths, on the microstructure and mechanical properties of the Ti6Al4V-ELI (Extra Low Interstitial) samples manufactured via L-PBF and grown in different build orientations. The effects of sandblasting process on both the mechanical performance and surface topography were analyzed. Finally, the correlation between the Vickers hardness and the tensile strength were analyzed considering the effects of the α-phase orientations.

2. Material and Methods

An extra-low-interstitial pre-alloyed Ti6Al4V powder, consisting of gas atomized, spherical particles with a diameter between 20 and 60 μm, was used for the laser powder bed fusion process. The chemical composition of the powder is shown in Table 1, and it generally differs in oxygen and iron contents from the chemical composition of the Ti6Al4V. The main difference between Ti6Al4V-ELI and Ti6Al4V alloys is that in Ti6Al4V-ELI the maximum oxygen and iron contents are lowered to 0.13% and 0.25%, respectively, from 0.20% (oxygen) and from 0.30% (iron), as reported in ASTM F3001-14 and F2924-14 specifications.

Table 1. Chemical composition of Ti6Al4V-ELI powder (wt%)

Ti	Al	V	Fe	O	N	H	C
Bal.	6.47 %	4.06 %	0.21 %	0.09%	0.01 %	0.001 %	0.01%

All samples were manufactured in a SLM®280 facility (SLM Solutions AG, Lübeck, Germany) equipped with an IPG fibre laser. The powder bed was pre-heated at 80°C and purged with Argon to reduce oxygen concentration to 0.05%. Dog-bone samples, whose dimensions are illustrated

in Fig. 1a, are built on the platform at different orientations (Fig. 1b) with the legend shown in Fig. 1c. Specimens were produced with a scanning speed of 1250 mm/s, a laser power of 340 W, a hatch spacing of 0.12 mm and a layer thickness of 0.06 mm.

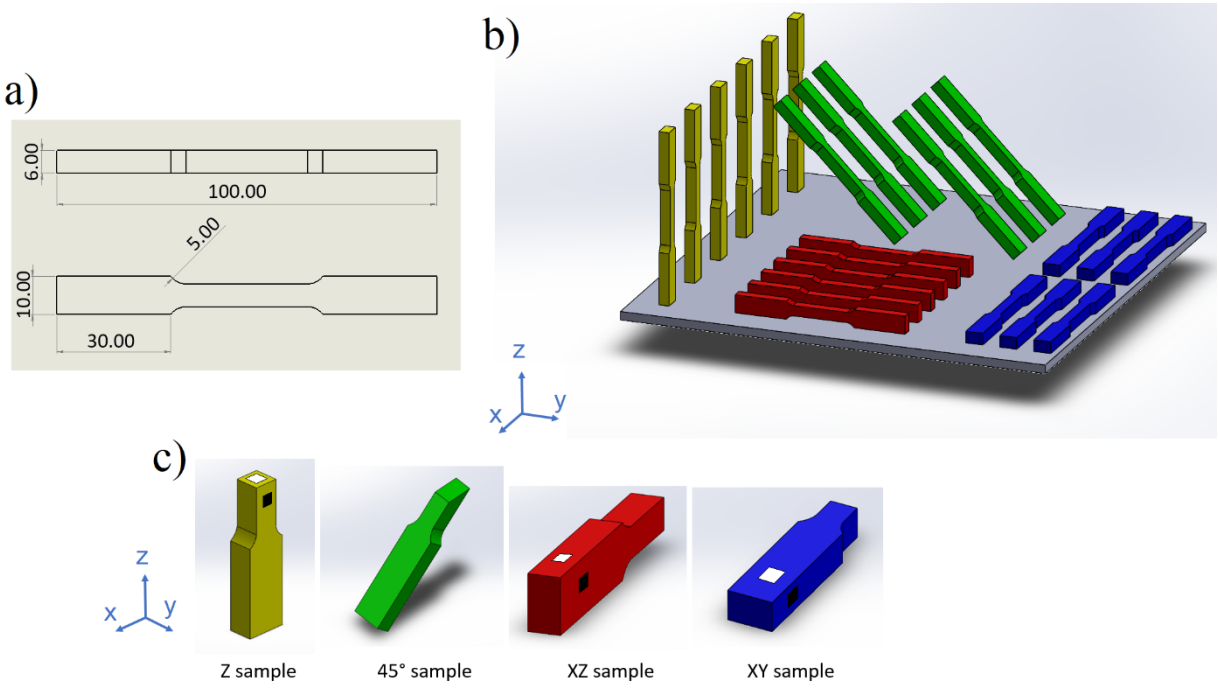

Figure 1. Schematic illustration of built samples: (a) dimensions in mm; (b) sample orientation on the built platform; (c) legend for samples (white and black squares indicate the 'xy' and 'xz' faces, respectively for Z, XZ and XY samples).

Thermal treatments were performed in a vacuum furnace and samples were cooled to room temperature with argon. A first batch of samples was heat treated at 704 °C for 120 min (704°C/120') and cooled to room temperature in one hour. This is a conventional heat treatment in accordance with the AMS 2801b standard. A second batch was kept at 740°C for 130 min (740°C/130'), cooled to 530°C in 90 min and then to room temperature in 60 min. This non-standard treatment was designed with the aim of increasing ductility and reducing the anisotropy of the mechanical properties through the higher peak temperature, which should favour more complete conversion of the α' phase into α+β, and the accompanying slow cooling stage, which should prevent stress accumulation and re-generation of α' phase.

After both heat treatments, a set of tensile samples was manually sand blasted (SB) at 0.3 m distance, using glass microspheres in the range of 200 ÷ 300 μm. Heat treated samples without the subsequent sand blasting are marked as 'no-SB'. Surface roughness was measured with a 3D optical profilometer (Taylor Hobson CCI MP-L, Leicester, UK) based on interferometry technology.

Tensile tests were performed at room temperature at a cross-head speed of 1 mm/min (Zwick Z100, ZwickRoell, Ulm, Germany) after both heat treatments (704°C or 740°C) and with the 'no-SB' and 'SB' surface finishing. In both cases, three samples were tested for each direction to obtain an associated error. Moreover, Vickers microhardness was measured on the surface and in the cross sections of the specimens (Leica VMHT, Wetzlar, Germany) at 500 g-load and 15 s-indentation time (ASTM E92-17).

For optical microscopy investigation, samples were mechanically ground, polished with a colloidal suspension and etched by Kroll's reagent (100 mL H_2O + 2 mL HF + 4 mL HNO_3) [27]. Image analysis was carried out by a light microscope (Leica DMi8, Wetzlar, Germany) equipped with the LAS AF-X software on the planes marked as 'xz' (black area) and 'xy' (white areas) of Fig. 1c. The thickness of the α-phase was measured according to the method proposed by Vander Voort et al. [28], who suggested to draw a circle of known radius (R) on the micrographs and to calculate the number (M) of intersections between the circumference and the α lamellae. Considering the circumference length ($2\pi R$) and the number M, the α-phase width (N_α) can be calculated through the following ratio

$$N_\alpha = 2\pi R / M \ . \quad (1)$$

Phase analysis was performed by a X'Pert PRO PANAlytical diffraction system, equipped with a Cu-Kα radiation source operating at 40 kV and 40 mA. XRD patterns were acquired in 2θ° from 30° to 90° with a scan step of 0.0167° (solid state detector array with an angular arch step of 2.1° and 200 s/step). The patterns were then matched to the ICDD JCPDF-2 database using X'Pert HighScore Plus software.

SEM investigations were performed on Z and XZ samples by a Nova NanoSEM 450 (FEI – Thermo Fischer Scientific, Hillsboro, Oregon, USA) equipped with energy-dispersive X-ray (EDX) spectroscopy. Sample surface was polished with a 3 μm polycrystalline diamond suspension and ≈60 nm-sized colloidal silica. Electron backscattered diffraction (EBSD) maps were also acquired on the same samples using an e⁻Flash 1000 detector (Bruker Nano GmbH, Berlin, Germany). In addition to the preparation described above, samples for EBSD mapping were further vibro-finished (Vibromet2, Buehler, Berlin, Germany) for 12 h using colloidal silica (MasterMet2, Buehler, Berlin, Germany) to remove any possible amorphization layer induced by the previous grinding steps. EBSD maps with a 320×240-pixel resolution were acquired at 400× magnification (15 kV-beam voltage and 20 ms-acquisition time per point). Based on the results of XRD patterns, the EBSD patterns were indexed to either the α-Ti (hcp) or β-Ti (bcc) phases. EBSD data was analysed both with the Esprit 2.1 software (Bruker Nano GmbH, Berlin, Germany) and with the MTEX package v. 5.7.0 [29] running under Matlab v. 2018b.

3. Results

3.1. Defects analysis and surface roughness

Porosity values are quite neglectable in all the investigated samples; in fact, the minimum and the maximum values measured in the cross-sections of dog-bone samples were 0.11 and 0.29% (vol. %) respectively, regardless of their build direction. The results are in accordance with Kasperovich et al. [30], who used process parameters like those in this work. Although the samples exhibited high density, two different kinds of pores were found: gas pores (Fig. 2a) with spherical shape (1-100 μm) and lack-of-fusion pores (Figs. 2b,c,d) elongated in the 'xy' plane (> 100 μm).

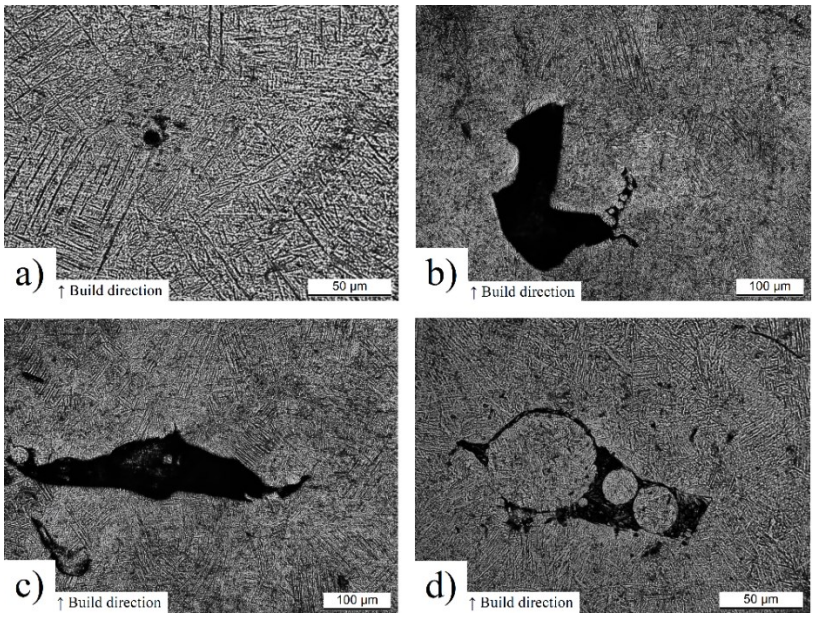

Figure 2. Optical micrographs showing (a) a gas pore and (b-d) different lack-of-fusion pores.

The surface roughness of a Z sample investigated in the 'xz' plane, before and after sand blasting (SB), is shown in Fig. 3 through a comparison between the 3D optical profilometer and SEM images.

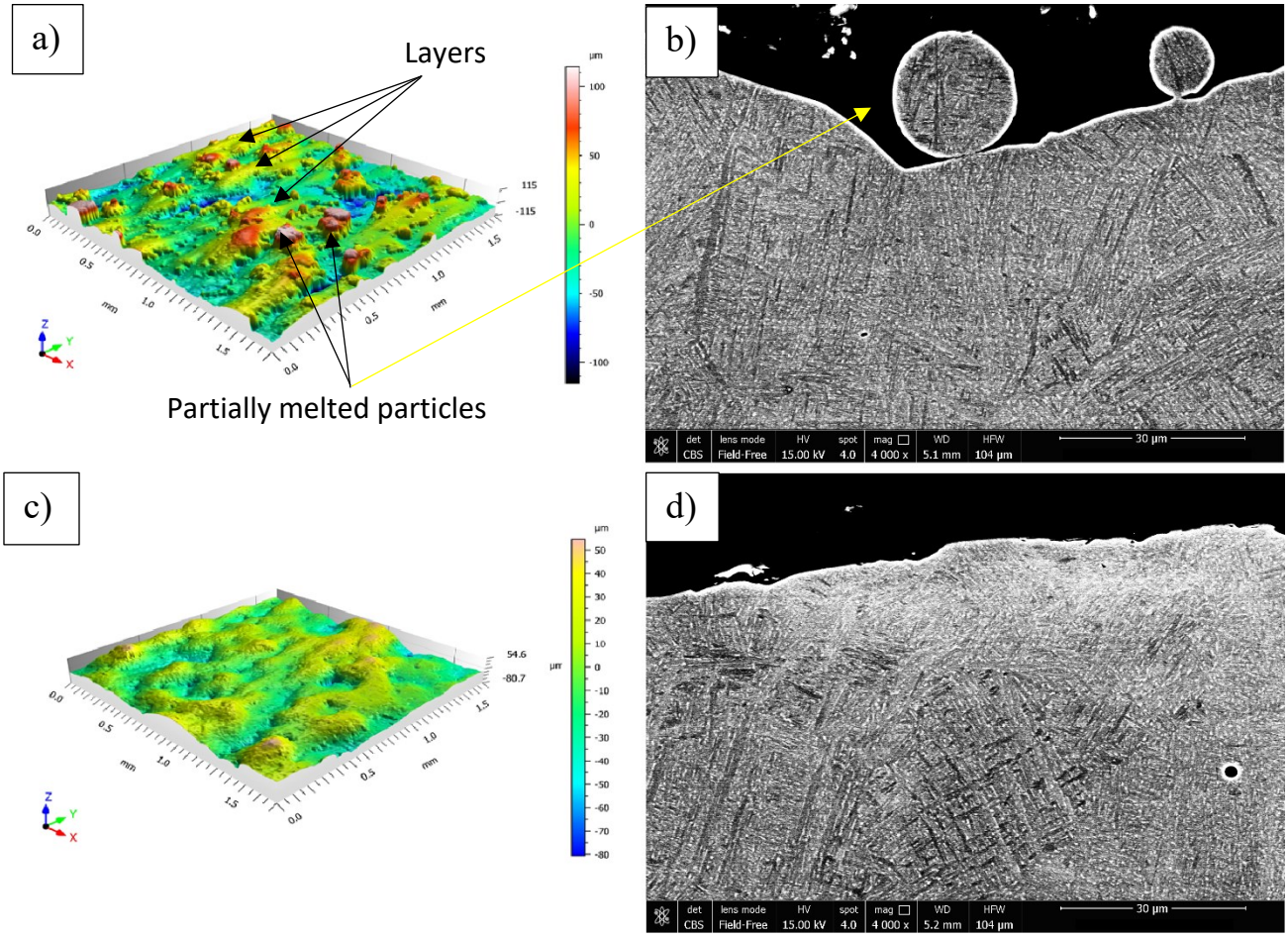

Figure 3. 3D surfaces (left column) and SEM micrographs (right column) of (a,b) samples with no-Sand Blasting 'no-SB' and (c,d) after sand-blasting 'SB'. The blue arrows represent the build direction.

Fig. 3a is a 3D-topographical map showing the traces of the laser scan before sand blasting (no-SB), which is consistent with the literature [9,23,25]. Particularly prominent peaks with rounded morphology were attributable to partially melted powder particles, as confirmed by the SEM micrograph in Fig. 3b. Fig. 3c is the 3D-map of the sand blasted (SB) sample showing a surface roughness reduction, as confirmed also in Fig. 3d. The measured values of average surface roughness (Ra) listed in Table 2 are close to 20 µm in the 'no-SB' samples, and are lower than those reported in literature [23,31]. This might depend on the specific processing conditions adopted in this work, including the characteristics of the feedstock powder and the process parameters such as the layer thickness.

Table 2. Average of surface roughness Ra and Rz parameters for 'no-SB' and 'SB' samples after the heat treatments.

Thermal treatments	Samples directions	no-SB		SB	
		Ra (μm)	Rz (μm)	Ra (μm)	Rz (μm)
704 °C	Z	21 ± 2	191 ± 18	14 ± 1	117 ± 20
	45°	24 ± 6	251 ± 20	16 ± 5	167 ± 14
	XZ	20 ± 4	181 ± 20	15 ± 3	120 ± 19
	XY	20 ± 3	240 ± 19	14 ± 3	130 ± 20
740 °C	Z	17 ± 1	130 ± 22	17 ± 4	120 ± 13
	45°	20 ± 6	240 ± 28	18 ± 5	158 ± 14
	XZ	21 ± 3	171 ± 18	15 ± 4	120 ± 21
	XY	21 ± 3	199 ± 15	14 ± 3	111 ± 19

The sandblasting process reduces the roughness of the 'SB' samples to approximately 15 μm: this is mainly due to the removal of the partially melted particles which were poorly attached to the surface. The same occurrence has been reported in [9,32].

Sandblasting did not visibly affect the microstructure of the heat-treated samples: SEM micrographs did not show any alteration, even in proximity of the outer surface (Figs. 3b and d). However, XRD patterns (Fig. 4) acquired on the surfaces of the 'SB' samples revealed a considerable broadening of the diffraction peaks. This means that, although the grains were not visibly deformed, they accumulated plastic strain in the near-surface area, within a depth at least comparable to the X-ray penetration depth (the attenuation length of the Cu-Kα radiation at $2\theta = 63.6°$ is approximately 6 μm).

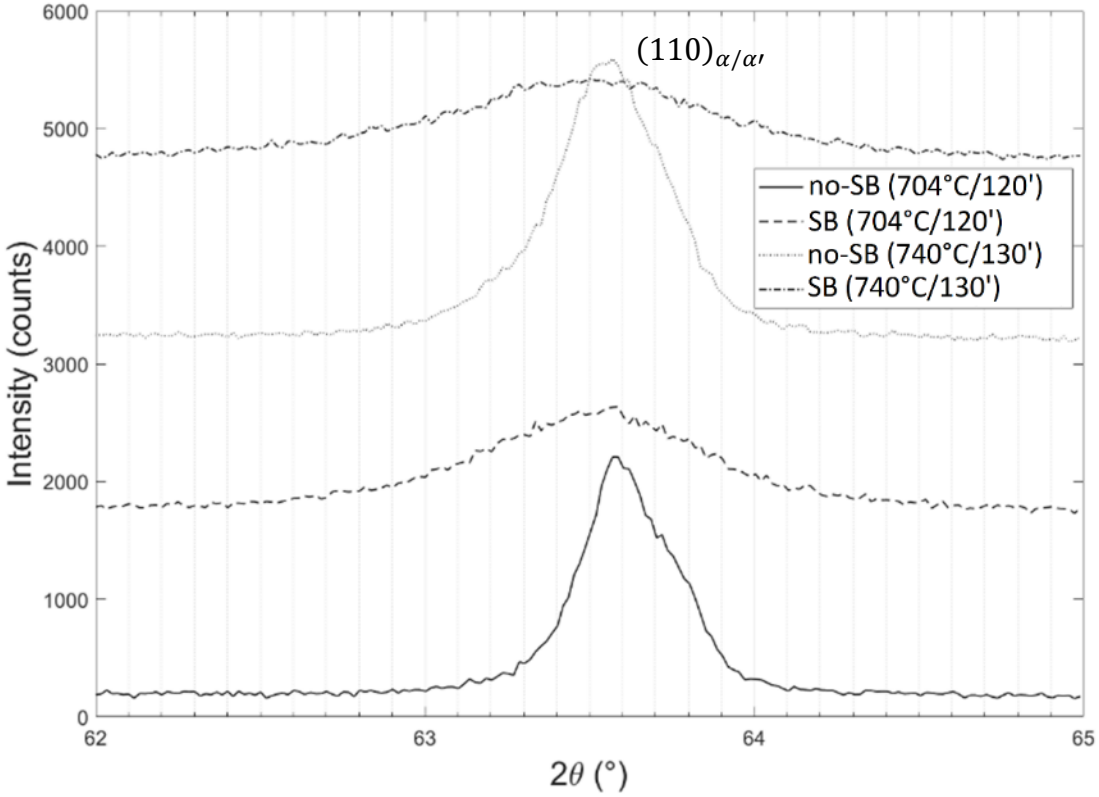

Figure 4. XRD patterns acquired on the 'xz' faces of 'no-SB' and 'SB' samples (Z orientation) for both the heat treatments.

3.2. Microstructure

Fig. 5 illustrates the microstructure of the as built Ti6Al4V-ELI Z sample. Fig. 5a shows the cross-sections of the molten pools in the 'xz' plane with elongated prior columnar β-grains visible along the build direction. On the 'xy' plane, perpendicular to the build direction, the nearly equiaxed cross-section of the prior columnar β-grains are marked by dashed contours (Fig. 5b) while dotted lines highlight the laser scan tracks. A fine acicular microstructure is recognizable at high magnification within these columnar β-grains.

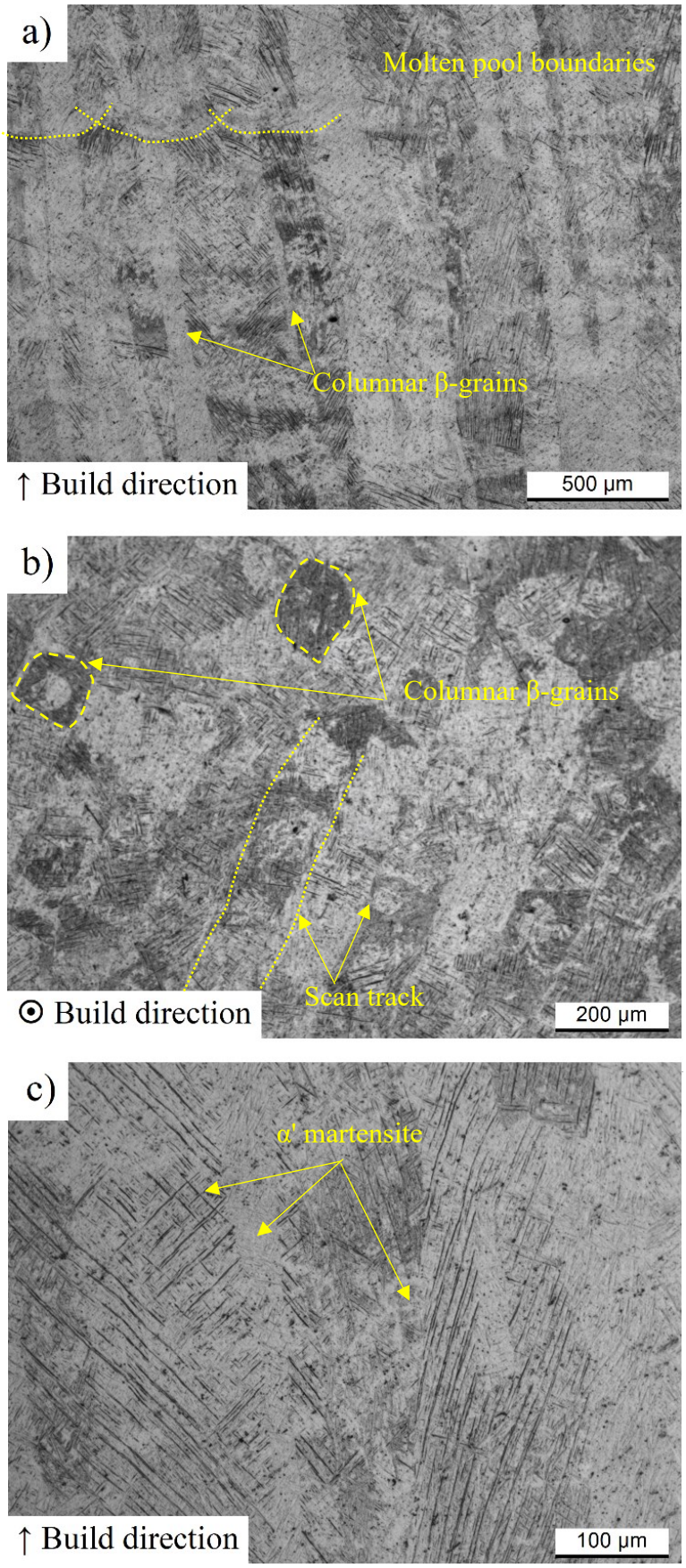

Figure 5. Optical micrographs of the as-built Ti6Al4V-ELI microstructure: grain morphology (a) along and (b) perpendicularly to the build direction; (c) a'martensite on the 'xy' plane.

The polyhedral section of the columnar β-grains remained visible on the 'xy' plane even after heat treatments performed below the β-transus at 704°C/120' (Fig. 6a for the Z sample) and at 740°C/130' (Fig. 6b for the sample built at 45°).

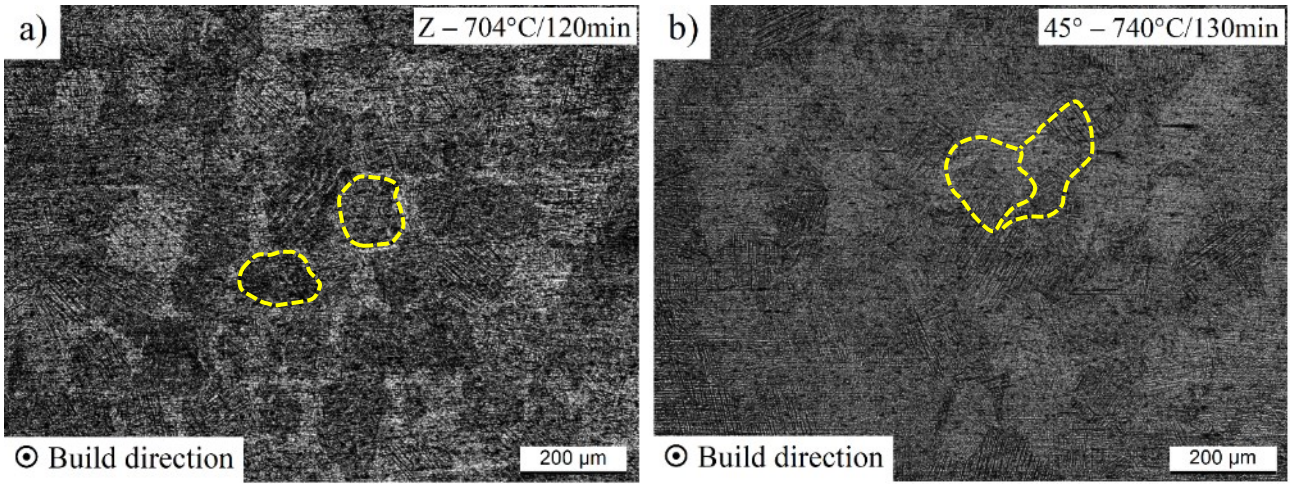

Figure 6. Optical micrographs showing the grain microstructure in the 'xy' planes of the (a) Z sample after 704°C/120min and of the (b) 45° sample after 740°C/130min.

For clarity of presentation, the dog-bone sample grown along the 45°-direction was cut along the perpendicular direction with respect to the z-axis (as illustrated in Fig. 1b); by this way, the micrographs reported in Fig. 6b represents the 'xy' plane as for the 'Z' sample.

The magnified SEM micrographs of the 'xy' planes for the Z sample (Figs. 7a,b) and the 'xz' planes for the XZ sample (Figs. 7c,d) after heat treatments at 704 °C (left column) and at 740 °C (right column) showed a fine, "cross-hatched" morphology similar to the one reported in [33] after a heat treatment at 800 °C for 1 h.

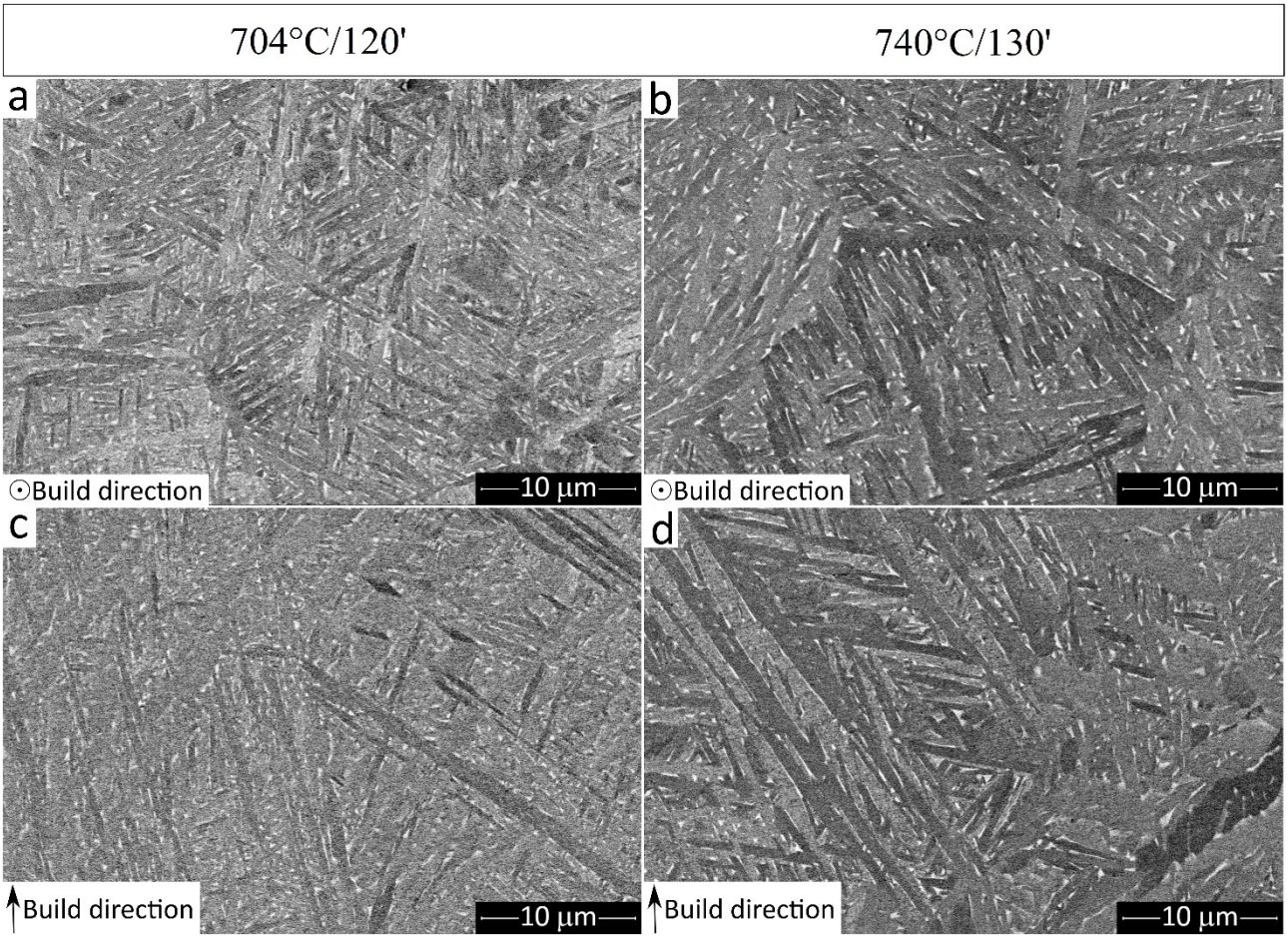

Figure 7. SEM micrographs showing the microstructure after heat treatments at 704°C/120' (left column) and 740°C/130' (right column) of: (a) and (b) 'xy' sections for the Z samples; (c) and (d) 'xz' planes of the XZ samples. The build direction is indicated on each image.

The "cross-hatched" microstructure is characterized by acicular phases with 45°-orientation with respect to one another. These acicular phases have darker contrast in backscattered electron imaging mode and are Al-rich (Fig. 8a: spectrum 2), and they are separated by a phase with brighter contrast, rich in vanadium and also containing some Fe (Fig. 8a: spectrum 1).

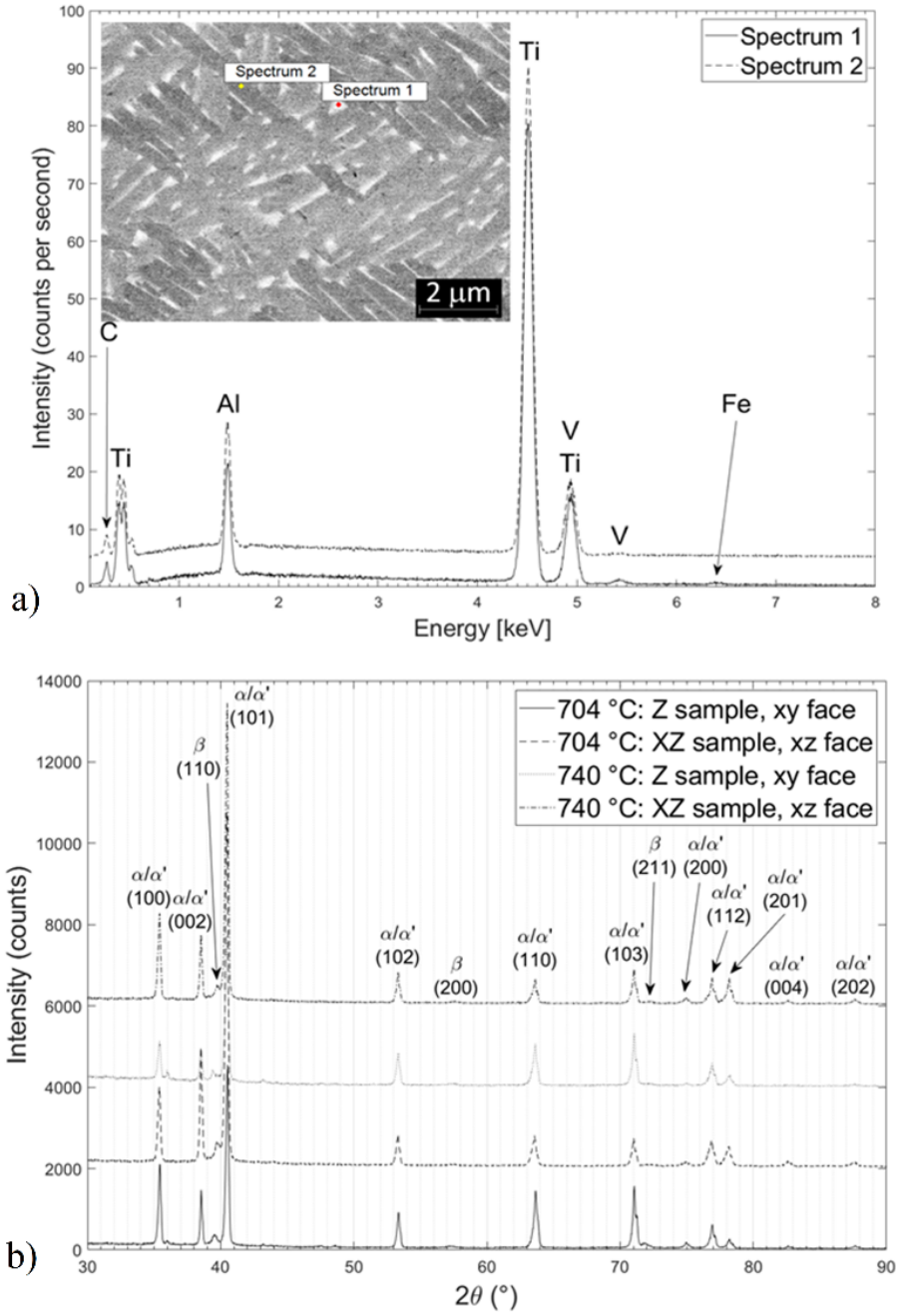

Figure 8. (a) EDX spectra investigations on the 'xy' section (Z sample) of '704°C/120' sample and (b) XRD patterns acquired on 'xy' and 'xz' sections of '704°C/120' and '740°C/130' samples.

XRD patterns (Fig. 8b) showed minor diffraction peaks of the β phase after both heat treatments. The analysis of EBSD maps (Fig. 9) also indicated the presence of 2–3% of β-phase in both heat-treated samples, irrespective of the treatment conditions. This result is quite consistent with the literature. Cao et al. [34] reported β volume fractions in the range from 1.50% (at 700 °C for 2 h) to 4.99% (at 800 °C). Moreover, the EBSD maps show that the "cross-hatched", Al-rich phase is an

α-phase. The columnar morphology of prior β-grains is also still identifiable in the inverse pole figure maps in Figs. 9a and c and Figs. 9b and c, respectively, meaning that the acicular α-phase has different orientations within different prior β-grains.

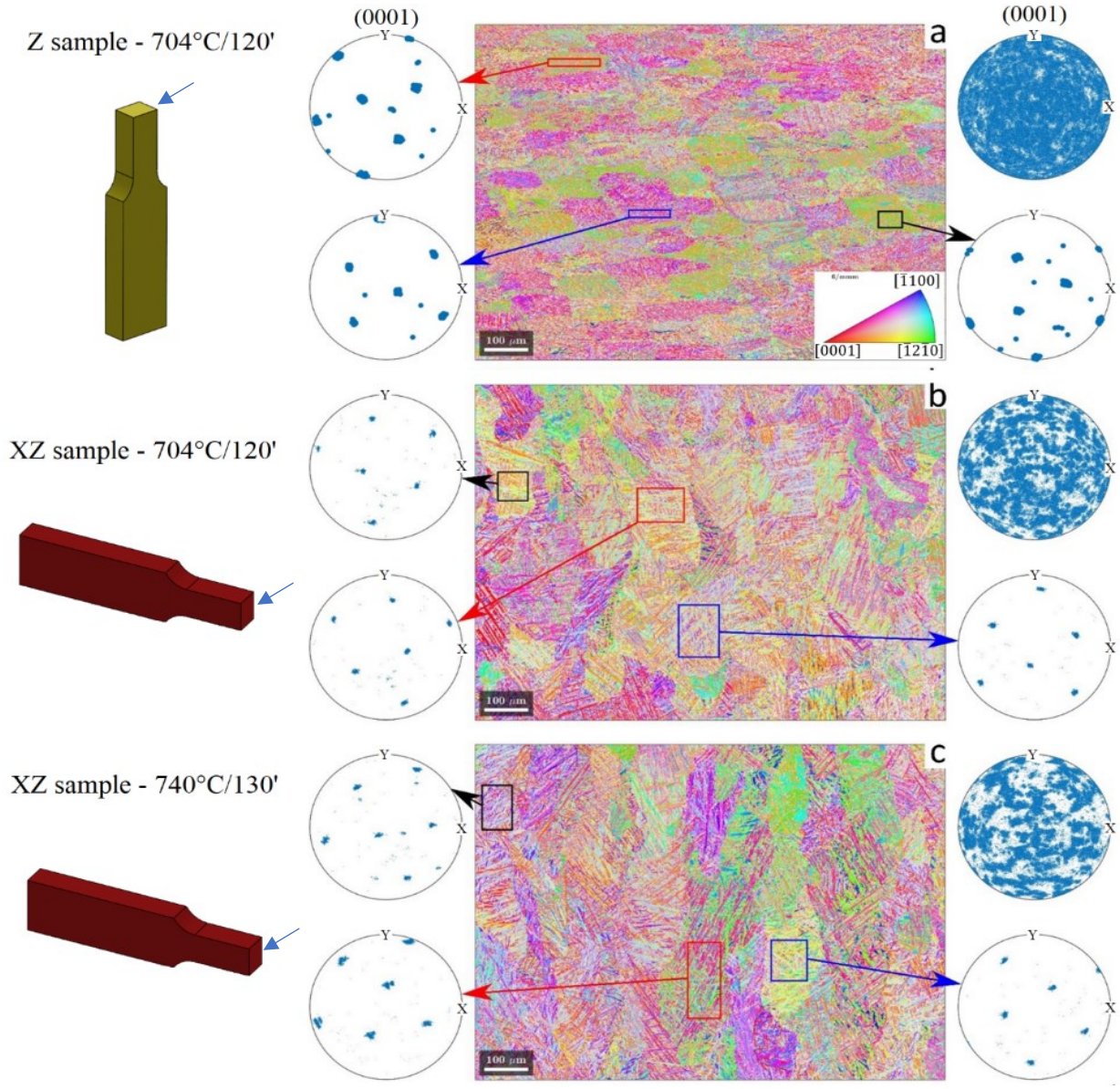

Figure 9. EBSD maps (inverse pole figures along the out-of-plane direction) acquired on (a) the'xy' section of the Z '704°C/120' sample, (b) on the 'xz' section of the XZ '704 °C/120' sample and on (c) the 'xz' section of the XZ 740°C/130' specimen. Scalebar length is 100 μm in all panels. Pole figures related to the <0001> direction of the hexagonal α-Ti phase are provided both for the entire map and for individual prior β-grains, marked on the maps.

Indeed, within each single prior β-grain, pole figures show that the hexagonal α-phase always assumed well-defined orientations (Fig. 9: rectangles show the areas where pole figures for the

<0001> direction of the hexagonal unit cell along the out-of-plane direction were extracted). This means that there is an orientational relation between the α-phase and the parent β-phase.

On the other hand, overall pole figures for the <0001> direction over the entire imaged areas show α-grains uniformly distributed along all spatial orientations (Fig. 9). Namely, the pole figures indicated that the α-phase did not have any preferential orientation when the analysis encompassed a sufficiently large number of prior β-grains. All crystallographic orientations of the α-phase were equally represented on both 'xy' (Fig. 9) and 'xz' (Fig. 9b and c) views, both parallel and perpendicular to the build direction. XRD patterns did not suggest any significant preferential orientation, either (Fig. 8b).

3.3 Mechanical properties after heat treatments

After both heat treatments, ultimate tensile and yield strength values decreased with respect to the as built ones (Figs. 10a and b), consistently with the literature [22,35,36], while the elongation to fracture increased after heat treatments (Fig. 10c).

Specifically, ultimate tensile strength and yield strength decreased by 10.4% and 9.7% on average, respectively, after the heat treatment at 704°C/120' and by 10.9% and 9.7% after exposure at 740°C/130' as compared to the as built values reported in [16,22,35,36]. This means that there were no substantial differences between tensile strengths after the two heat treatments.

As shown in Fig. 10, small differences among samples with different orientations could be seen for the ultimate tensile strength and yield strength after the 704°C/120' treatment. The UTS of the XZ and XY samples were higher than those of the 'Z' and '45°' samples by about 40 MPa, while the yield strength decreases from 975 to 925 MPa. There were two possible sources of anisotropy in the present samples: i) the elongation of the columnar prior β-grains along the build direction, and ii) the presence of lack-of-fusion pores on the 'xy' plane. They can be expected to have opposite effects on the mechanical properties. Considering the tensile strength and ductility values of all heat-treated

SB and no-SB samples, the minimum requirements dictated by the ASTM F3001-14 (UTS > 860 MPa, YS > 795 MPa, ε > 8%) are satisfied.

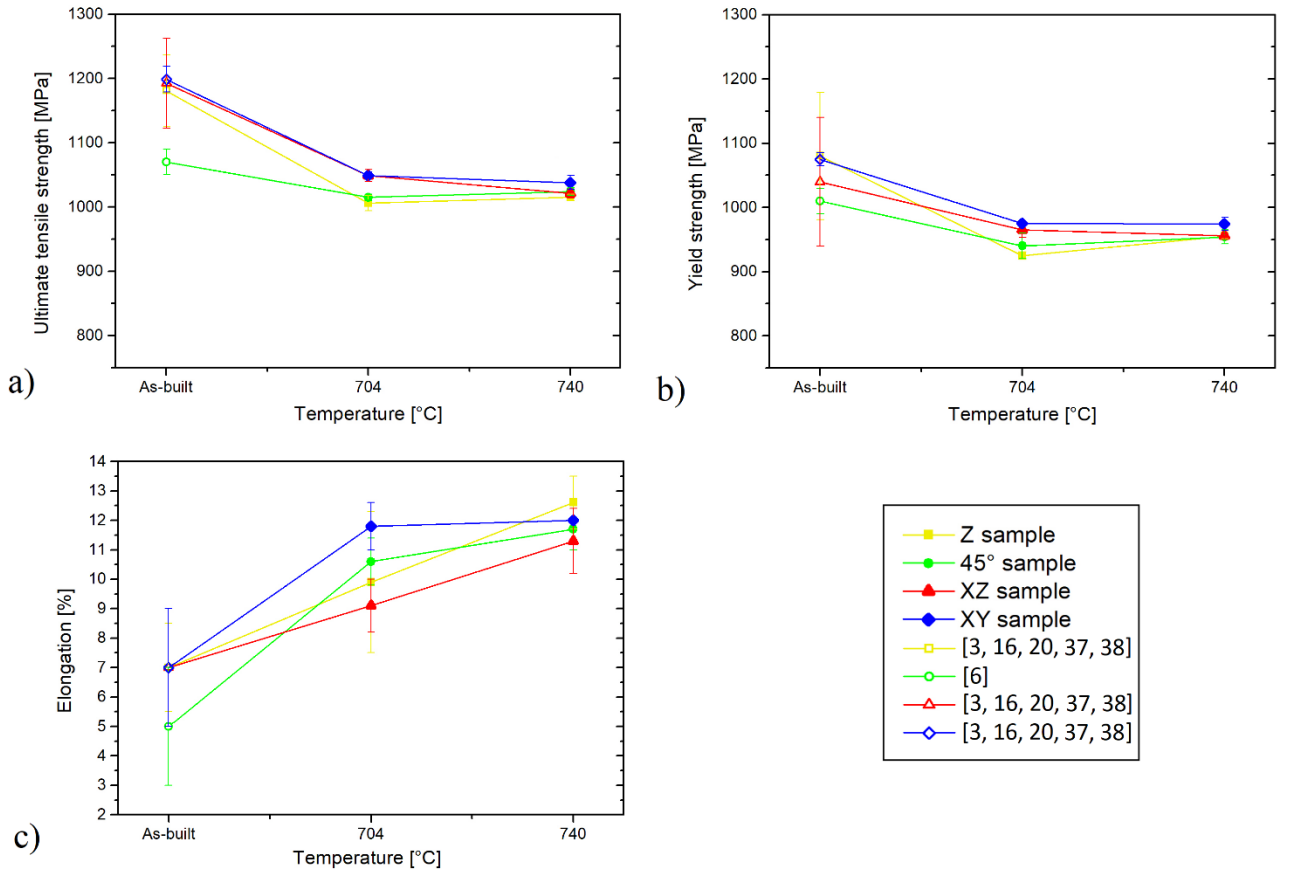

Figure 10. Tensile properties of Ti6Al4V-ELI samples in the as-built and heat-treated conditions: (a) UTS, (b) YS and (c) elongation to fracture. The empty symbols represent the average of the UTS, YS and elongation values reported in [3,6,16,20,37,38]

Finally, the sandblasting process did not influence the mechanical properties, as reported in Fig. 11a for tensile strengths and in Fig. 11b for the elongations to fracture, contrary to the expectations put forward in the Introduction section.

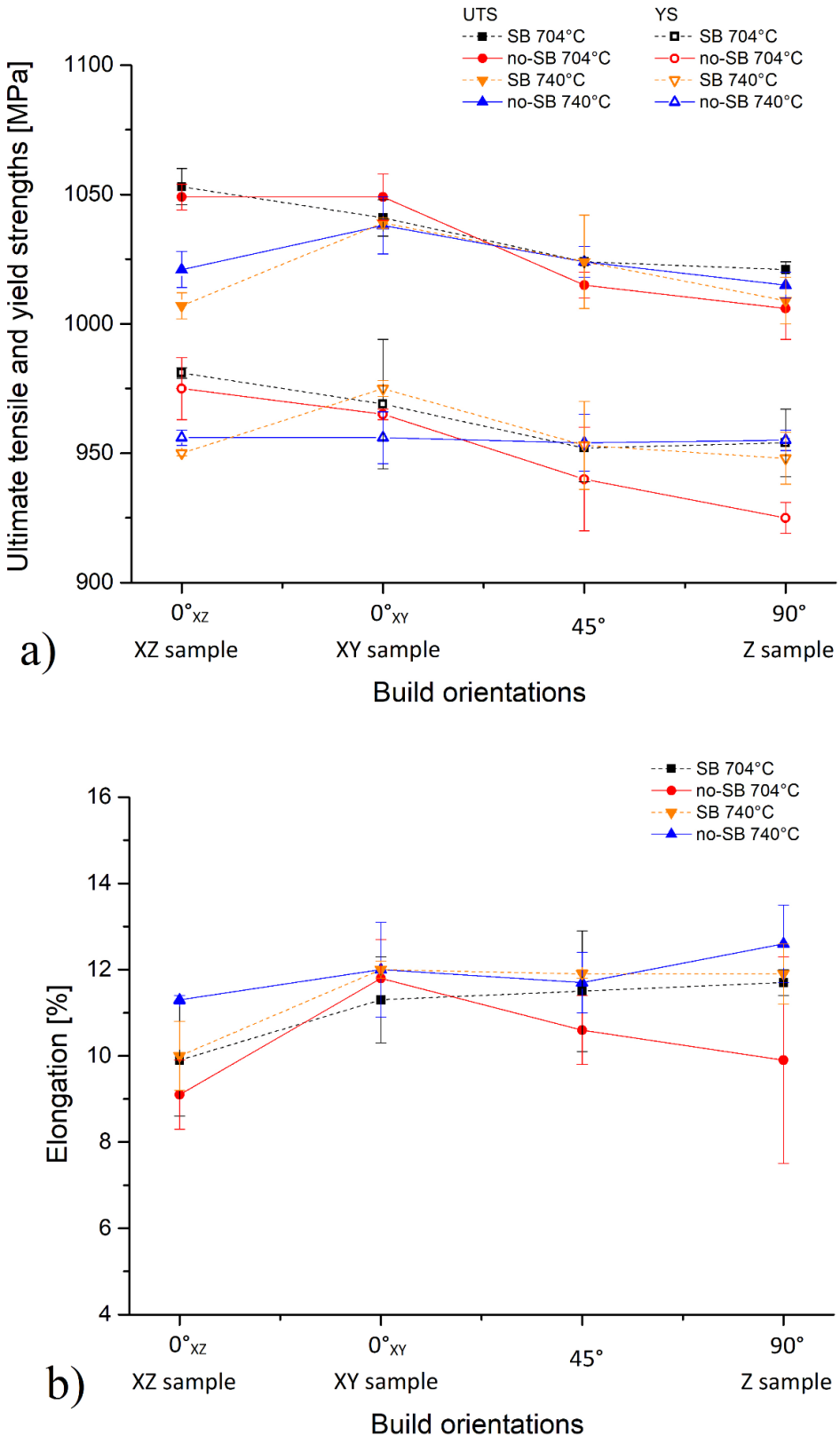

Figure 11. Mechanical properties of samples of different build orientations and surface finishing (no-SB: continuous lines, SB: dashed lines): (a) Ultimate tensile strength and yield strength and (b) elongation to fracture.

Table 3 shows the average HV microhardness of the ‘no-SB’ and ‘SB’ samples measured on their cross-sections.

Table 3. Average Vickers microhardness values of the heat-treated dog bone samples.

Build directions	704°C/120’		740°C/130’	
	no-SB	SB	no-SB	SB
Z	386 ± 9	385 ± 10	385 ± 8	382 ± 8
45°	381 ± 10	384 ± 11	372 ± 11	385 ± 7
XZ	400 ± 12	395 ± 9	384 ± 8	379 ± 9
XY	395 ± 7	388 ± 7	380 ± 7	388 ± 6

The average hardness values tended to decrease very slightly with increasing treatment time, although the differences were usually smaller than the associated error ranges, hence hardly significant. This confirmed the results of tensile tests discussed in Section 3.3 (Fig. 11). Comparable results were obtained in [39] before and after heat treatments under the β-transus (~ 1000 °C) and in [25], where the effects induced by the distance from the build platform for Ti6Al4V-ELI samples were analyzed.

4. Discussion

The as-built microstructure of Ti6Al4V-ELI samples is composed by α’-martensite contained within β-grains which possess columnar shape and are arranged along the Z-axis (i.e., the build direction) (Fig. 5a,b). The elongated shape of the β-grains along the Z-axis is related to the molten pool solidification. In fact, β-grain nucleation and growth depend on the ratio between thermal gradient and solidification rate during their complex thermal history [40,41]. In addition, the growth of β-grains tends to follow the heat fluxes, which are primarily oriented along the build direction as heat is conducted from the molten pool into the underlying layers, and the columnar grains that are formed in the previous layer ‘n-1’ also become the nuclei of the grains in the ‘n’ layer [42].

The high cooling rate (> 410 °C/s) that characterized the solidification process of the molten pool induces a complete transformation of such β-phase into α’ martensite as shown in Fig. 5c. In fact, at such rate the cooling curve intersected both the Ms line at 780 °C and the Mf line at 650 °C [4,16,22,43]. Below the Ms temperature, the bcc (body-centred cubic) lattice of the β-phase

transformed without diffusion to the hcp (hexagonal close packed) lattice of the α'-phase, inducing an increase of internal stress and a change in mechanical properties [21,44]. Therefore, primary α' (length > 20 μm), secondary α' (length 10 – 20 μm), tertiary α' (length 1 – 10 μm) and quartic α' (length < 1 μm) phases can be identified [3,8,17,37]. These kinds of α' martensitic phases are accordingly formed at high cooling rates: if the rate exceeds 410 °C/s the transformation β → α' is complete, but if the cooling rate is between 410 °C/s and 20 °C/s, it does not [16,45]. Primary α' martensite is created within prior β-grains formed along the build direction. The other types of α' are generated by subsequent thermal cycles during the laser powder bed fusion process, as the pre-existing α' martensite variants are partly or entirely converted to new β phase and then cooled at high rate again to form new α' phase [17]. These kinds of α' martensite arranged perpendicular to each other within the prior columnar β-grains [17,21].

After the heat treatments at 704°C/120' and 740°C/130', the magnified SEM micrographs (Figs. 7a,b and Figs. 7c,d, respectively) show that the orthogonal arrangement of the different variants was preserved, but the α' phase was, in fact, mostly converted into α-phase.

Evidence that the cross-hatched microstructures of Fig. 7 are composed largely of α phase, i.e. that the α' phase decomposed into an α+β mixture after the heat treatments, is provided by the presence of V, Fe-rich areas along the boundaries of the acicular, Al-rich α phase. In fact, α'-martensite is supersaturated in β-stabilizers because it is formed from the parent β phase through a diffusionless, displacive transformation. Therefore, when α'-martensite decomposes, it segregates the β phase rich in V and Fe along its own grain boundaries [33,46]. The "cross-hatched" morphology of this α+β mixture is similar to the one reported in [33] after a heat treatment at 800 °C for 1 h.

In this scenario, some authors have accordingly identified the temperature range between 600 °C and 750 °C for the decomposition of α' martensite [25,47,48]. More specifically, it is thought that the decomposition of α' martensite is inhibited at temperatures below 550 °C [43] by twinning dislocations that are originally developed in the high-temperature β-phase during the L-PBF process.

Accordingly, Sallica-Leva et al. [33] showed that the α' → α + β transformation occurs at 715 °C, which is reasonably close to the lowest treatment temperature that we employed in this work (704 °C). In support of this, Rafi et al. [36], Zhao et al. [43] and Haar et al. [49] and confirmed that the α' → α + β transformation begins at 705 °C.

A partial α' → α+β decomposition after the heat treatments was also reported in [34,46]. Spigarelli et al. [50] showed that the transformation is indeed partial, not complete, by highlighting the presence of α'-martensite (~ 25-28%) in the α-laths contained in the same heat-treated samples discussed in the present work.

In accordance with [49], we therefore inferred that the α-phase found in the heat-treated samples was not directly produced from the parent β-phase, but it resulted from the decomposition of α'-martensite. Therefore, it can be assumed that the crystal lattice of the α-phase fully retained the orientation of α' martensite when the latter decomposed by expelling the excess of V and Fe, as previously discussed. If this is true, starting from the EBSD maps of the α-phase, it should be possible to reconstruct the parent β-phase by applying the known orientational relation between β and α', in the hypothesis that the same orientational relation was retained when α' turned into α. The orientational relation is $(110)_{\beta} \parallel (0001)_{\alpha'}$ and $[11\,\bar{1}]_{\beta} \parallel [2110]_{\alpha'}$ [16,51]. EBSD data was post-processed using a procedure specifically devised to reconstruct parent β from the orientational relation mentioned above [52], implemented in the MTEX software [29]. From the misorientation among different α grains, the procedure tells whether they belonged to the same parent β grain or to distinct ones [52]. Figs. 12a, b and c show the reconstructed maps of the parent β phase, and, for better clarity, the grain boundaries of the parent β phase are also re-plotted (Fig. 12d, e and f) onto the original maps of the α phase, repeated from Fig. 9. The reconstructed maps prove that the procedure did correctly identify the prior β-phase boundaries, confirming the above hypothesis on the preservation of the α'-martensite orientation in the α-phase. Finally, on the 'xy' surface (perpendicular to the build direction) the reconstruction procedure made it graphically apparent that the prior β-grains were lined up regularly (Fig. 12a), probably reflecting the laser scanning direction. All this indicates that the

memory of the prior β-grains was fully preserved after the heat treatments below the β-transus. Interestingly, the reconstruction of the pole figures of the parent β-phase along the <001> direction (Figs. 12g,h and i) shows that, despite its columnar morphology, it did not grow with a preferential crystallographic orientation. Namely, different crystallographic directions are aligned along the columnar axis in different parent β-grains. This explains why, in turn, the α phase has no preferential orientation on the macro-scale, as noted above.

Image analysis performed on magnified SEM micrographs (Fig. 7) indicated a slight but perceivable coarsening of the α-phase, whose width increased from (540 ± 60) nm at 704°C/120' to (700 ± 10) nm (at 740 °C/130') due to the increase in temperature and to the slow furnace cooling down to 530 °C performed after the 740°C/130'. This, however, has clearly not impaired the preservation of the orientational relation, as specified above. In addition, the same heat treatments did not affect the size of the prior β-grains, which are not influenced by the coarsening effects. In fact, the average lengths of the columns are (110±15) μm and (120±20) μm after the heat treatments at 704 °C and 740 °C, respectively. The values are similar (within error range) to those found in as built conditions (100±20) μm and to those reported in [43,53].

704°C/120’		740°C/130’
‘xy’ section of the Z sample	*‘xz’ section of the XZ sample*	*‘xz’ section of the XZ sample*

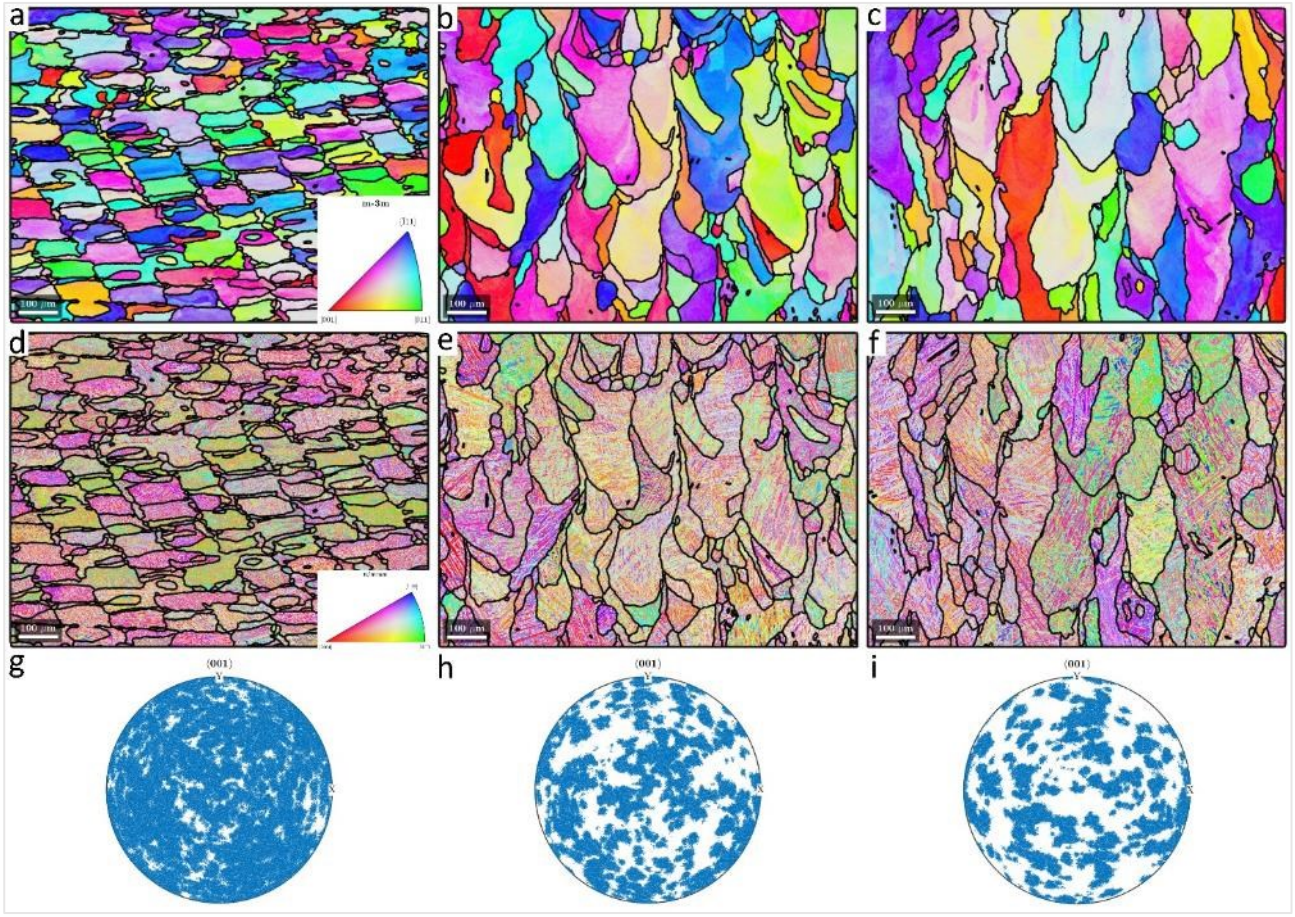

Figure 12. Mathematically reconstructed EBSD maps (inverse pole figures along the out-of-plane direction) of the parent β phase (first row), the corresponding original maps with superimposed parent β grain boundaries (second row) and reconstructed <001> pole figures of the parent β phase (third row) for: (a,d,g) the ‘xy’ section of the Z ‘704°C/120’ sample; (b,e,h) the ‘xz’ section of the XZ ‘704°C/120’ sample and (c,f,i) for the ‘xz’ section of the XZ ‘740°C/130’ sample. Scalebar length is 100 µm in panels a - f.

In relation to the mechanical properties, the slight coarsening of the α-phase after the 740°C/130’ (its width increased by 160 nm on average, as mentioned above) thus had no measurable effect. Moreover, the morphology and the relative amounts of the α and β grains were the same after both heat treatments, which contributed to the absence of any substantial differences between the tensile strengths measured after the two heat treatments, as noted in Section 3.3.

In order to clarify the relation between α-phase width and mechanical strength, a plot of yield strength vs. α-phase width was constructed using the present results as well as a variety of literature data from diverse sources (Fig. 13). The relationship of the yield strength (σ_y) with the grain size fits well (red symbols in Fig. 13) with the general trend inferred from literature values as reported in [7,10,22,37,54].

This trend is consistent with Eq. (2) (Hall-Petch equation):

$$\sigma_y = \sigma_0 + \mu/\sqrt{D} \tag{2}$$

where σ_0 is the intrinsic strength [MPa], μ is the strengthening coefficient [MPa $m^{1/2}$] and D is the average grain size [m], intended in this manuscript as the thickness of the α lamellae. Eq. (2) is traditionally used for casting alloys, where the average grains size is typically bigger than alloys manufactured via the L-PBF process. However, Zhang et al. [55] emphasized that Eq. (2) can be applied to the Ti6Al4V-ELI alloy manufactured by electron beam powder bed fusion process, L-PBF and directed energy deposition.

Therefore, a dependence of yield strength on α-phase width exists, but the present samples have too close grain size values to produce a measurable change, considering the magnitude of the slope of the plot in Fig. 13 (i.e. the actual value of the strengthening coefficient) and the scatter of the data.

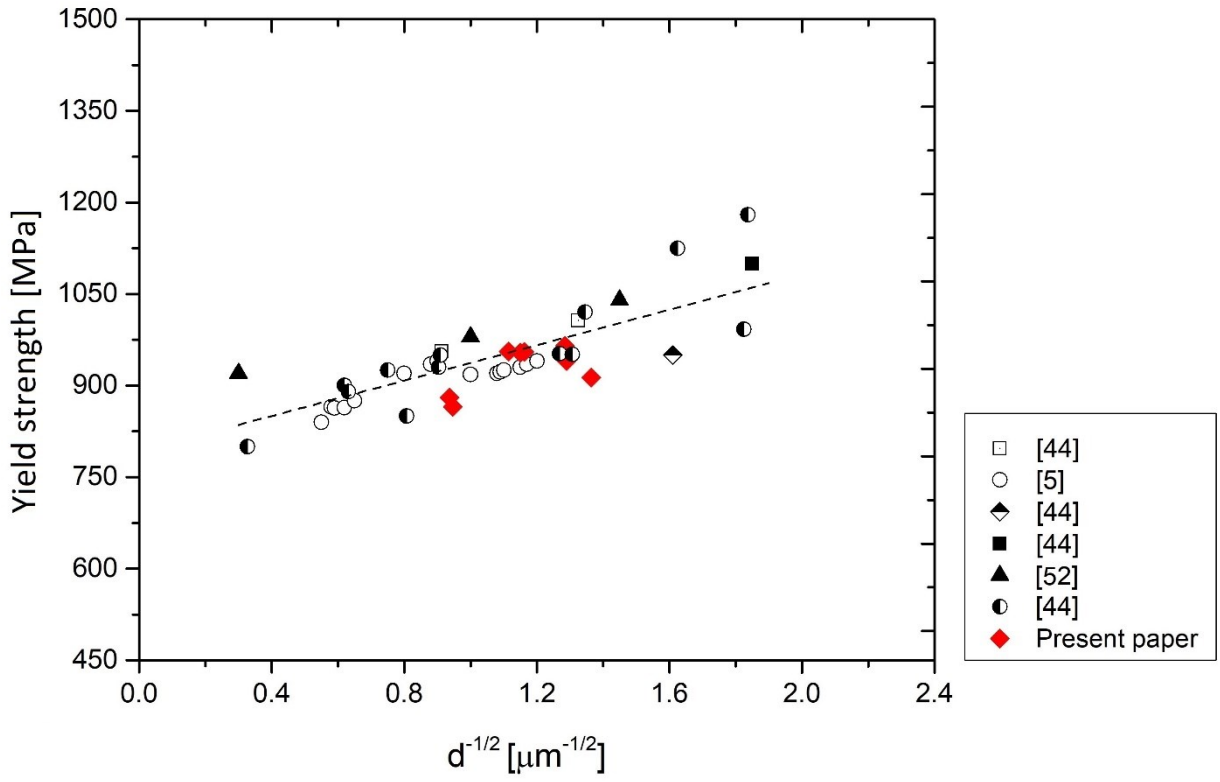

Figure 13. Yield strength versus average grain size.

In addition, the lack of preferential orientation of the α-phase at the macro-scale, yielding more or less equally represented directions for all α-phase crystals, explains why samples manufactured along different build directions had comparable tensile behaviour.

Minor differences between XZ, XY and Z, 45° samples can be caused either by the relationship between the load direction and the LOF orientations, and/or between the load direction and the columnar β-grains [16]. In the latter case, the elongation of the columnar prior β-grains can be expected to result in higher strength for samples loaded along the build direction (i.e. higher strength for the Z samples), whilst lack-of-fusion pores elongated on the xy plane can compromise the mechanical strength of samples loaded along the build direction. The fact that the strength of the Z and 45° samples was slightly lower after the 704°C/120' treatment suggests that the latter effect was prevalent. It should be reminded that some authors [34] reported higher tensile strength for samples built along the Z direction, contrary to the present results. This might be due microstructural differences resulting from distinct laser powder bed fusion process parameters. The choice of these optimized process parameters (P, v, h, t) is the first step to obtain high-quality or fully dense samples, but the attention could be focused on other parameters as: the composition of the gas contained in the build chamber and its impenetrability, the powder chemical composition, the shape and size of the particles, etc … [16,56]. In this context, the argon contained within the gas atomized Ti6Al4V powder [57], as well as the unavoidable gaps among particles within the powder bed, are sources of gas porosity. In fact, gas bubbles might be unable to escape the melt pool before solidification due to the high cooling rate. The formation of lack-of-fusion pores can be attributed to issues with the printing process, such as inhomogeneities and/or irregularities in the thickness of the powder bed, and to a low energy density [22,25,32,58]. The lack-of-fusion pores can be divided in three different types [57]: i) a gap without un-melted particles (Fig. 2b), ii) an elongated void containing un-melted powder particles (Fig. 2c) and iii) un-melted powder particles that separate the opposing pore faces (Fig. 2d). Because of their shape, lack-of-fusion pores are stress concentration points and create cracks which reduce the measured tensile strength [5,16,22,38]. Finally, pores can have different effects on

mechanical properties measured along different orientations. When the load is applied parallel to the build direction, the lack-of-fusion pores, being elongated on the xy plane, tend to open, causing the premature failure of tensile samples. Instead, if the loading axis is rotated by 90°, the pores tend to close except for LOF where its major axis is aligned with the load direction [16,22,38].

Finally, the variation of the ultimate tensile strength (square symbols) and the yield strength (circle symbols) were correlated in Fig. 13 with the type of microstructure previously discussed and with the values analyzed in [15,18,22,38]. Notably, the mechanical properties obtained after both heat treatments were consistent with those reported in the literature [16,18,22,38].

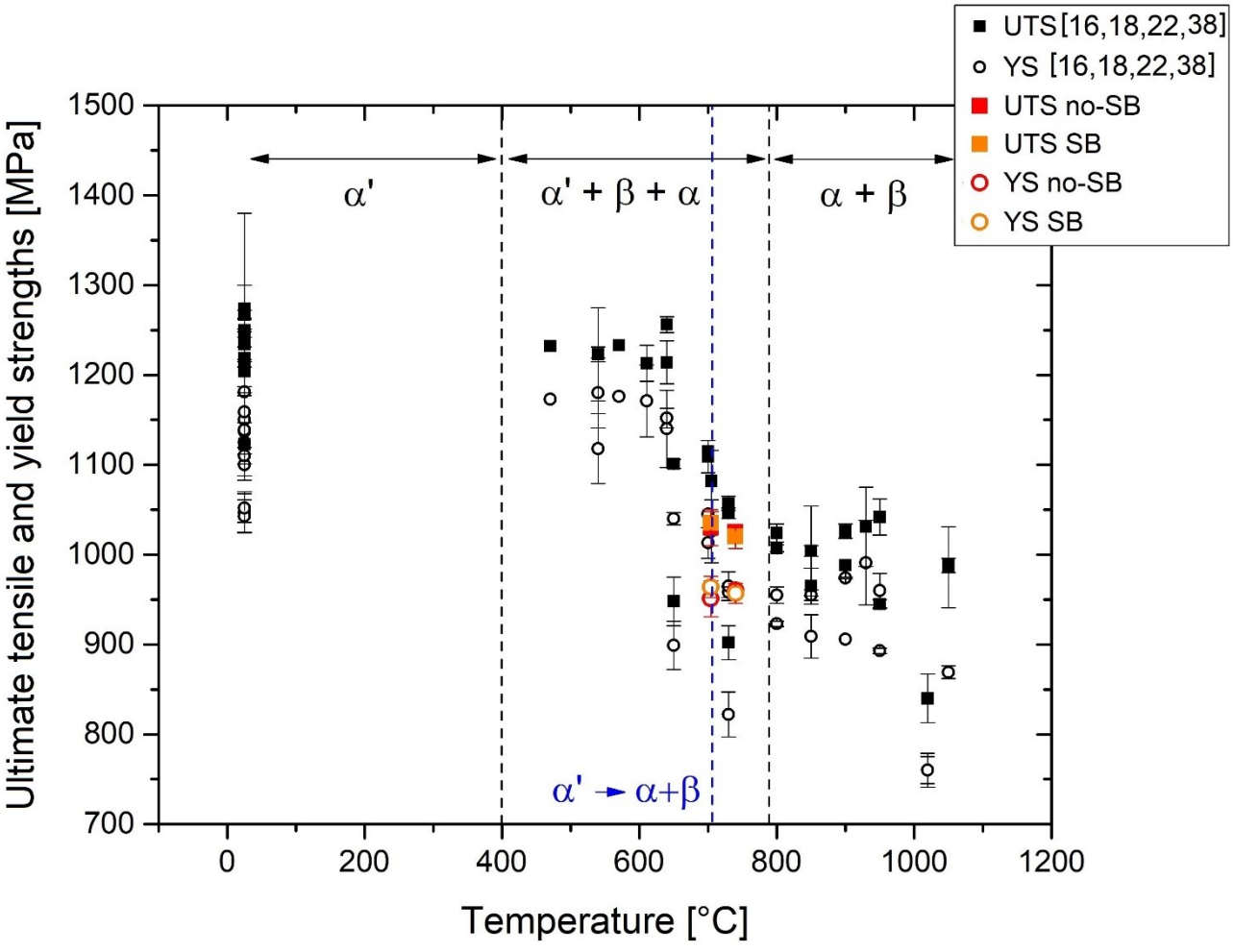

Figure 14. Tensile strength data of Ti6Al4V-ELI manufactured by laser powder bed fusion are illustrated as a function of heat treatment temperatures. The black symbols are data from literature [16,18,22,38], while the red and orange ones are from this work.

In the same context, the sandblasting process does not influence the mechanical properties as highlighted in Fig. 12 and by the full and empty orange symbols in Fig. 13. On the other hand, the

reduction of Ra values and the elimination of the particles on the sample surface (Fig. 3) confer several advantages in the biomedical field. Firstly, Ponader et al. [11] showed the positive effects on proliferation and differentiation of human osteoblasts with Ra values below 24.9 μm, also affirming that surface treatments are required. Vaithiling et al. [59] demonstrated that the immortalized NIH 3T3 mouse embryonic fibroblast cells were viable on both the polished and as-fabricated surface (Ra = 17.3 ± 3.7 μm) of Ti6Al4V samples by L-PBF. Secondly, Cox et al. [60] and Ginestra et al. [12] illustrated that the random presence of the agglomerates of particles on the sample surface facilitate tissue ingrowth but impede uniform cell distribution. At the same time, the removal of the finest particles (< 10 μm) can be appropriate due to their interaction with the giant cells, fibroblasts, macrophages, and osteoclasts and the subsequent inflammatory responses [61].

In relation to the space and aerospace sector, the Ra values listed in Table 2 do not reach satisfactory values for different applications in this field where Ra < 3.2 μm is required [62].

The Vickers microhardness test is widely used also to predict the yield strength of metallic materials such as steels and aluminium alloys. As regards the Ti6Al4V alloys, there are not many empirical relationships to evaluate the tensile strength. Hickey [63] proposed the following linear correlation for the cast Ti6Al4V alloy:

$$UTS = (HV/6.33) + 503 \quad (3)$$

where *UTS* and *HV* are the ultimate tensile strength and the Vickers microhardness, respectively. At the same time, Keist et al. [64] proposed strength-hardness relations for the Ti6Al4V alloy manufactured by direct energy deposition process highlighting the effect of α-phase orientations in as-built conditions and after the HIP (hot isostatic pressing) heat treatment. Surely, the contribution conferred by the α-phase on the Vickers hardness will be higher in a Ti6Al4V alloy manufactured through an AM process than in the same cast alloy due to the different content of the α-phase: 90-95% and 80-85%, respectively. No research in the literature proposed correlations between UTS, YS and HV for a Ti6Al4V alloy produced via an AM process based on powder bed fusion technique as L-PBF.

Also in this case, the α-phase orientations must be considered due to their fundamental impact on the mechanical behaviour [16,65,66]. In relation to the orientation of the hcp lattice structure, which characterized the α-phase, the hardness contribution varies. If the basal plane is perpendicular to the load direction, the obtained Vickers hardness values will be higher than those measured along other crystallographic orientations [67,68].

Starting from the empirical correlation between *HV* and mechanical properties, Tabor et al. [69] first showed that the representative plastic strain induced by the Vickers indentation is in the range between 8 and 10% and the corresponding stress value is approximatively described as *HV*/3 and *HV*/2.9 for copper alloys and steels, respectively. Secondly, based on power-law strain hardening ($\sigma_t = K\varepsilon_t^n$), where the true stress (σ_t) is a function of true strain (ε), strain exponent (n) and strength coefficient (K), Cahoon et al. [70] suggested an improvement of the relation between Vickers microhardness and ultimate tensile strength:

$$UTS = (HV/2.9)(n/0.217)^n \quad (4)$$

where *UTS* is the ultimate tensile strength, *HV* is the Vickers microhardness value and *n* is the strain hardening exponent. Cahoon et al. [71] also analyzed the relationship between Vickers microhardness and yield strength suggesting the Eq. (5):

$$\sigma_y = (HV/3)(0.1)^n \quad (5)$$

where σ_y is the yield strength, *HV* is the Vickers microhardness value and *n* is the strain hardening exponent. As matter of fact, the strain hardening behaviour and the Hollomon's coefficients (*n*, *K*) of metallic materials manufactured by the AM processes have not been well characterized in the literature [64]; therefore, this topic needs to be deepened. In the present paper, Hollomon's coefficients were determined according to the ASTM standard E464 and all values are shown in Table 4. Similarly, the previously discussed equations are not widely used within the AM field due to the microstructural complexity of the manufactured alloy. In this context, the structure of the Ti6Al4V-ELI manufactured via laser powder bed fusion process consists of a great quantity of α-phase (EBSD

maps in Fig. 9 indicate 97÷98%), so this phase dominates the microhardness measurements. In addition, the HV values are strictly correlated to the preferential or random orientation of the α-phase. Keist et al. [64] highlighted that the strength values obtained from microhardness by applying Cahoon's equation to Ti6Al4V-ELI alloys manufactured via directed energy deposition process were lower than the measured values. They suggested an improvement to Cahoon's equations by the following corrections:

$$UTS = \left(\frac{HV}{2.9A}\right)\left(\frac{n}{0.217}\right)^{n} \quad (6)$$

$$\sigma_y = \left(\frac{HV}{3A}\right)(0.1)^{n} \quad (7)$$

where A is the impact factor of the α-phase orientation on mechanical properties. They showed impact factors of 1.14 and 1.10 for the ultimate tensile strength and yield strength, respectively, after the hot isostatic pressing (HIP) heat treatment, while values of 1.08 and 1.06 were proposed for samples subjected to a stress relief heat treatment at 650 °C for 240 min. This implied that the α-phase orientation increases the hardness by 10 - 14% in the HIP heat-treated samples and by 6 - 8% in the stress relieved samples.

Table 4. Mechanical properties of heat-treated samples for 'no-SB' and 'SB' samples.

HTs	Dir.	E [GPa]	UTS [MPa]		YS [MPa]		elongation [%]		*n*		*K* [MPa]	
			no-SB	***SB***	***no-SB***	***SB***	***no-SB***	***SB***	***no-SB***	***SB***	***no-SB***	***SB***
704°C/120'	Z	107 ± 3	1006 ± 12	1021 ± 3	925 ± 6	954 ± 13	9.9 ± 2.4	11.7 ± 0.3	0.06	0.05	916 ± 6	1005 ± 7
	45°	103 ± 3	1015 ± 5	1024 ± 18	940 ± 20	952 ± 13	10.6 ± 0.8	11.5 ± 1.4	0.05	0.05	968 ± 12	992 ± 16
	XZ	106 ± 1	1049 ± 9	1053 ± 7	965 ± 2	981 ± 2	9.1 ± 0.9	9.9 ± 1.3	0.05	0.05	1006 ± 15	990 ± 16
	XY	111 ± 2	1049 ± 5	1041 ± 7	975 ± 12	969 ± 25	11.8 ± 0.8	14.3 ± 1.0	0.05	0.05	967 ± 10	1020 ± 20
740°C/130'	Z	109 ± 4	1015 ± 5	1009 ± 9	955 ± 4	948 ± 10	11.4 ± 0.9	11.9 ± 0.7	0.05	0.04	984 ± 2	982 ± 8
	45°	110 ± 1	1024 ± 6	1024 ± 18	954 ± 11	953 ± 17	11.4 ± 0.8	11.9 ± 0.1	0.04	0.05	967 ± 28	990 ± 17
	XZ	109 ± 1	1021 ± 7	1007 ± 5	956 ± 3	950 ± 3	10.4 ± 1.1	10.0 ± 0.8	0.05	0.05	971 ± 17	993 ± 10
	XY	117 ± 2	1038 ± 11	1039 ± 2	974 ± 10	975 ± 1	11.0 ± 0.1	12.1 ± 0.2	0.04	0.04	998 ± 12	974 ± 13

The mathematical fit of the experimental data with equations (6) and (7) returned 'A' impact factors of 1.21 for the UTS and 1.22 for the yield strength. The graphical representation in Fig. 15 confirms that the unmodified Cahoon's Eqs. (4) and (5) do not best correlate the tensile strength

values and Vickers microhardness (continuous lines). The best fit is obtained by the dotted lines representing Eq. (6) with A = 1.22 and Eq. (7) with A = 1.21 and with n = 0.05.

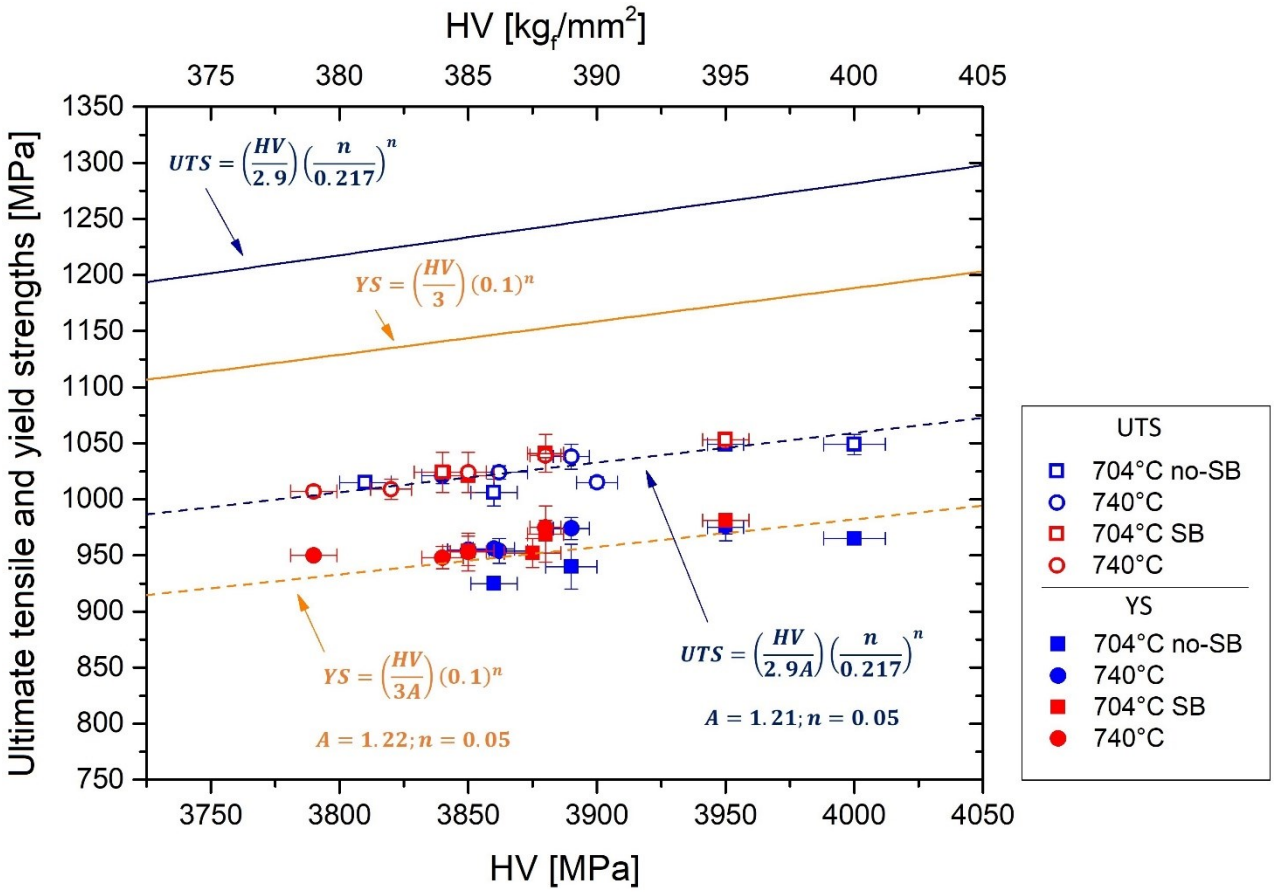

Figure 15: Vickers microhardness as a function of ultimate tensile strength and yield strength- measured from Ti6Al4V-ELI produced by laser powder bed fusion process. The black lines are related to the models indicated by Chaoon et al. [70,71], while the orange lines are related to the present work.

5. Conclusions

The present paper investigated the microstructure and the mechanical properties of Ti6Al4V-ELI samples fabricated via laser powder bed fusion process along different orientations (Z, 45°, XZ and XY) and subsequently subjected to two heat treatments: a standard one at 704 °C for 120 min and a non-standard one at 740 °C for 130 min. In both cases, half of the samples were sand blasted and the effects of this surface treatment on the microstructure and the mechanical properties were also investigated.

The main conclusions are as follows:

1. The α’ phase was partially transformed into α+β after the 704 °C/120 min and 740 °C/130 min treatments, with analogous amounts of β-phase despite the different peak temperatures and cooling paths.
2. The α phase formed by decomposition of α’ martensite maintained the lattice orientation of the latter without any rotation; therefore, there still was an orientational relation between the α phase and the parent β-grains after the heat treatments. On the macro-scale, however, the α-phase exhibited no preferential orientation regardless of the different build orientations of the samples. This implies that the prior β-grains also exhibited no preferential crystallographic orientation despite their columnar morphology.
3. The sandblasting process also did not visibly alter both the microstructure and the mechanical properties of different sets of samples. Its effects were only visible through the enlargement of the diffraction peaks.
4. Accordingly, there was hardly any evidence of anisotropy in the mechanical response of the samples as characterized through Vickers microhardness and tensile testing. Where present, anisotropy seemed to be more related to some elongated pores between layers than to the columnar texture of the prior β-grains.
5. The microstructure of the heat-treated Ti6Al4V ELI samples is characterized by α-phase lamellae without a preferential orientation as highlighted by the EBSD measurements. This microstructural texture causes a discrepancy of about 21-22% between the actual mechanical strength values of the samples and those predicted from the microhardness measurements using Cahoon’s equations. These empirical equations between the Vickers microhardness and the tensile strengths can therefore be applied to Ti6Al4V alloy manufactured by laser powder bed fusion only if an impact factor (A) term is added.

Acknowledgements

The authors greatly acknowledge Beam-it (Fornovo di Taro, PR) for supplying materials

Conflicts of Interest

The authors declare no conflict of interest during the preparation of the present research paper.

References

[1] ASTM F2792-12a, Standard Terminology for Additive Manufacturing Technologies, West Conshohocken, PA, USA, 2012.

[2] A. Olleak, Z. Xi, Simulation of layer-by-layer Selective Laser Melting process with an efficient remeshing technique, Procedia Manuf. 24 (2019) 613-618. https://doi.org/10.1016/j.promfg.2019.06.167

[3] A.M. Khorasani, I. Gibson, U.S. Awan, A. Ghader, The effect of SLM process parameters on density, hardness, tensile test and surface quality of Ti6Al4V, Addit. Manuf. 25 (2019) 176-186. https://doi.org/10.1016/j.addma.2018.09.002

[4] L. Thijs, F. Verhaeghe, T. Craeghs, J.V. Humbeeck, J.P. Kruth, A study of the microstructural evolution during selective laser manufacturing of Ti-6Al-4V, Acta Mater. 58 (2010) 3303-3312. https://doi.org/10.1016/j.actamat.2010.02.004

[5] M. Simonelli, Y.Y. Tse, C. Tuck, Effect of the building orientation on the mechanical properties and fracture modes of SLM Ti-6Al-4V, Mater. Sci. Eng. A 616 (2014) 1-11. https://doi.org/10.1016/j.msea.2014.07.086

[6] M. Donachie, Titanium: A technical guide, second ed., ASM International, 2000.

[7] L.E. Murr, S.A. Quinones, S.M. Gaytan, M.I. Lopez, A. Rodela, E.Y. Matrinez, D.H. Hernandez, E. Martinez, F. Medina, R.B. Wicker, Microstructure and mechanical behavior of Ti-6Al-4V produced by rapid-layer manufactured, for biomedical applications, J. Mech. Behav. Biomed. Mater. 2 (2009) 20-32. https://doi.org/10.1016/j.jmbbm.2008.05.004

[8] I. Yadroitsev, P. Krakhmalev, I. Yadroitsava, A. Du Pcessis, Qualification of Ti6AL4V ELI alloy produced by Laser Bed Powder Fusion for Biomedical Applications, JOM 70 (2018) 372-377. https://doi.org/10.1007/s11837-017-2655-5

[9] P. Jamshidi, M. Aristizabal, W. Kong, V. Villapun, S. Cox, L. Grover, M. Attallah, Selective Laser Melting of Ti-6Al-4V: The Impact of Post-Processing on the Tensile, Fatigue and Biological Properties for Medical Implant Applications, Materials. 13 (12) (2020) 2813-2829. https://doi.org/10.3390/ma13122813

[10] S. Nag, R. Banerjee, Laser deposition and deformation behavior of Ti-Nb-Zr-Ta alloys for orthopedic implants, J. Mech. Behav. Biomed. Mater. 16 (2012) 21-28. https://doi.org/10.1016/j.jmbbm.2012.08.014

[11] S. Ponader, E. Vairaktaris, P. Heinl, C.v. Wilmowsky, A. Rottmair, C. Körner, R.F. Singer, S. Holst, K.A. Schlegel, F.W. Neukam, E. Nkenke, Effects of topographical surface modifications of electron beam melted Ti-6Al-4V titanium on human fetal osteoblasts, J. Biomed. Mater. Res. 84A (4) (2008) 1111-1119. https://doi.org/10.1002/jbm.a.31540

[12] P. Ginestra, R.M. Ferraro, K Zohar-Hauber, A. Abeni, S. Giliani, E. Ceretti, Selective Laser Melting and Electron Beam Melting of Ti6Al4V for Orthopedic Applications: A Comparative Study on the Applied Building Direction, Materials. 13 (23) (2020) 5584. https://doi.org/10.3390/ma13235584

[13] R. Boyer, G. Welsh and E. Colling, Materials properties Handbook, ASM International, 1994.
[14] A.E. Wilson-Heid, S. Qin, A.M. Beese, Anisotropic multiaxial plasticity model for laser powder bed fusion additively manufactured Ti-6Al-4V, Mater. Sci. Eng. A. 738, 90-97. https://doi.org/10.1016/j.msea.2018.09.077
[15] X. Zhao, S. Li, M. Zhang, Y. Liu, T.B. Sercombe, S. Wang, Y. Hao, R. Yang, L.E. Murr, Comparison of the microstructures and mechanical properties of Ti-6Al-4V fabricated by selective laser melting and electron beam melting, Mater. Des. 95 (2016) 21-31. https://doi.org/10.1016/j.matdes.2015.12.135
[16] E. Ghio, E. Cerri, Additive Manufacturing of AlSi10Mg and Ti6Al4V Lightweight Alloys via Laser Powder Bed Fusion: A Review of Heat Treatment Effects, Materials. 15 (6) (2022) 2047. https://doi.org/10.3390/ma15062047
[17] J. Yang, H. Yu, J. Yin, M. Gao, Z. Wang, X. Zeng, Formation and control of martensite in Ti-6Al-4V alloy produced by selective laser melting, Mater. Des. 108 (2016) 308-318. https://doi.org/10.1016/j.matdes.2016.06.117
[18] B. Vrancken, L. Thjis, J. Kruth, J. Humbeeck, Heat treatments of Ti6Al4V produced by Selective Laser Melting: Microstructure and mechanical properties, J. Alloys Compd. 541 (2012) 177-185. https://doi.org/10.1016/j.jallcom.2012.07.022
[19] M. Frkan, R. Konecna, G. Nicoletto, L. Kunz, Microstructure and fatigue performance of SLM-fabricated Ti6Al4V alloy after different stress-relief heat treatments, Transp. Res. Proc. 40 (2019) 24-29. https://doi.org/10.1016/j.trpro.2019.07.005
[20] X.Y. Zhang, G. Fang, S. Leeflang, A.J. Boettger, A.A. Zadpoor, J. Zhou, Effect of subtransus heat treatment on the microstructure and mechanical properties of additively manufactured TI-6Al-4V alloy, J. Alloys Compd. 735 (2018) 1562-1575. https://doi.org/10.1016/j.jallcom.2017.11.263
[21] N. Kazantseva, P. Krakhmalev, M. Thuvander, I. Yadroitsev, N. Vinogradova, I. Ezhov, Martensitic transformation in Ti-6Al-4V (ELI) alloy manufactured by 3D Printing, Mater. Charact. 146 (2018) 101-112. https://doi.org/10.1016/j.matchar.2018.09.042
[22] T. Vilaro, C. Colin, J.D. Bartout, As-fabricated and Heat-treated microstructures of the Ti-6Al-4V alloy processed by Selective Laser Melting, Metall. Mater. Trans. A 42 (2001) 3190-3199. https://doi.org/10.1007/s11661-011-0731-y
[23] P. Edwards, M. Ramulu, Fatigue performance evaluation of selective laser melted Ti-6Al-4V, Mater. Sci. Eng. A 598 (2014) 327-337. https://doi.org/10.1016/j.msea.2014.01.041
[24] M. Jamshidinia, R. Kovacevic, The influence of heat accumulation on the surface roughness in powder-bed additive manufacturing, Surf. Topogr. 3 (2015) 014003. https://doi.org/10.1088/2051-672X/3/1/014003
[25] H. Gallaraga, D.A. Lados, R.R. Dehoff, M.M. Kirka, P. Nandwana, Effect of the microstructure and porosity of Ti-6Al-4V ELI alloy fabricated by electron beam melting (EBM), Addit. Manuf. 10 (2016) 47-57. https://doi.org/10.1016/j.addma.2016.02.003
[26] Y.Y. Sun, S. Gulizia, C.H. Oh, D. Fraser, M. Learly, Y.F. Yang, M. Qian, The influence of as-built surface conditions on mechanical properties of Ti-6Al-4V Additive Manufacturing by Selective Electron Beam Melting, JOM 68 (2016) 791-799. https://doi.org/10.1007/s11837-015-1768-y

[27] L. Nádai, B. Katona, A. Terdik, E. Bognar, Chemical etching of titanium samples, Period. Polytech. Mech. Eng. 57(2) (2013) 53-57. https://doi.org/10.3311/PPme.7046
[28] G.F.V. Voort, A. Roósz, Measurement on the interlamellar spacing of perlite, Metall. 17 (1984) 1-17. https://doi.org/10.1016/0026-0800(84)90002-8
[29] F. Bachmann, R. Hielscher, H. Schaeben, Texture analysis with MTEX – Free and Open source software toolbox, Solid state phenom. 160 (2010) 63-68. https://doi.org/10.4028/www.scientific.net/SSP.160.63
[30] G. Kasperovich, J., Hausmann, Improvement of fatigue resistance and ductility of Ti6Al4V processed by Selective Laser Melting, J. Mater. Process. Technol. 220 (2015) 202-214. https://doi.org/10.1016/j.jmatprotec.2015.01.025
[31] M.F. Sadali, M.Z. Hassan, F. Ahmad, H. Yahaya, Z.A. Rasid, Influence of selective laser melting scanning speed parameter on the surface morphology, surface roughness and micropores for manufactured Ti6Al4V parts, J. Mater. Res. 15 (2020) 2025-2035. https://doi.org/10.1557/jmr.2020.84
[32] H. Gong, K. Rafi, H. Gu, T. Starr, B. Stucker, Analysis of defect generation in Ti-6Al-4V parts made using powder bed fusion additive manufacturing processes, Addit. Manuf. 1-4 (2014) 87-98. https://doi.org/10.1016/j.addma.2014.08.002 .
[33] E. Sallica-Leva, R. Caram, A. Jardini, J. Fogagnolo, Ductility improvement due to martensite α' decomposition in porous Ti-6Al-4V parts produced by sleective laser melting for orthopedic implants, J. Mech. Behav. Biomed. Mater. 54 (2016) 149-158. https://doi.org/10.1016/j.jmbbm.2015.09.020
[34] S. Cao, R. Chu, X. Zhou, K. Yang, Q. Jia, C.V.S. Lim, A. Huang, X. Wu, Role of martensite decomposition in tensile properties of selective laser melted Ti-6Al-4V, J. Alloy Compd. 744 (2018) 357-363. https://doi.org/10.1016/j.jallcom.2018.02.111
[35] F. Nalli, L. Bottini, A. Boschetto, L. Cortese, F. Veniali, Effect of industrial heat treatment on the mechanical performance of Ti6Al4V processed by Selective Laser Melting, Appl. Sci. 10 (7) (2020) 2280. https://doi.org/10.3390/app10072280
[36] H.K. Rafi, N.V. Karthik, H. Gong, T.L. Starr, B.E. Stucker, Microstructures and Mechanical Propreties of Ti6Al4V parts fabricated by Selective Laser Melting and Electron Beam Melting, J. Mater. Eng. Perform. 22 (2013) 3872-3883. https://doi.org/10.1007/s11665-013-0658-0
[37] W. Xu, S. Sun, U. Elambasseril, Q. Liu, M. Brandt, M. Qian, Ti6Al4V additively manufactured by selective laser melting with superior mechanical properties, JOM 67(3) (2015) 668-673. https://doi.org/10.1007/s11837-015-1297-8
[38] P.H. Li, W.G. Guo, W.D. Huang, Y. Su, X. Lin, K.B. Yuan, Thermomechanical response of 3D laser-deposited Ti-6A6-4V alloy over a wide range of strain rates and temperatures, Mater. Sci. Eng. A 647 (2015) 34-42. https://doi.org/10.1016/j.msea.2015.08.043
[39] D. Wang, W. Dou, Y. Yang, Research on Selective Laser Melting of Ti6Al4V: Surface Morphologies, Optimized Processing Zone, and Ductility Improvement Mechanism, Metals. 8 (7) (2018) 471. https://doi.org/10.3390/met8070471
[40] S. Bontha, N.W. Klingbeil, P.A. Kobryn, H.L. Fraser, Thermal process maps for predicting solidification microstructure in laser fabrication of thin-wall structures, J. Mater. Process. Technol. 178(1-3) (2016) 135-142. https://doi.org/10.1016/j.jmatprotec.2006.03.155

[41] S. Gorsse, C. Hutchinson, M. Goune, R. Banerjee, Additive manufacturing of metals: a brief review of the characteristic microstructures and properties of steels, Ti-6Al4V and high entropy alloys, Sci. Technol. Adv. Mater. 18 (1) (2017) 584-610. https://doi.org/10.1080/14686996.2017.1361305

[42] A.A. Antonysamy, J. Meyer, P.B. Pragnell, Effect of build geometry on the β-grain structure and texture in additive manufacturing of Ti-6Al-4V by selective electron beam melting, Mater. Charact. 84 (2013) 153-168. https://doi.org/10.1016/j.matchar.2013.07.012

[43] Z.Y. Zhao, L. Li, P.K. Bai, Y. Jin, L. Wu, J. Li, R. Guan, H.Q. Qu, The Heat Treatment Influence on the Microstructure and Hardness of TC4 Titanium Alloy Manufactured via Selective Laser Melting, Materials. 11 (8) (2018) 1318-1320. https://doi.org/10.3390/ma11081318

[44] Y. Wada, N. Nakada, S. Onaka, Internal Stress of Plate Martensitic Depending on Aspect Ratio via fcc-hcp Martensitic Transformation in Metastable Austenitic Stainless Steels, Mater. Trans. 61(1) (2020) 61-67. https://doi.org/10.2320/matertrans.Mt-MJ2019007

[45] T. Ahmed, H.J. Rack, Phase transformation during cooling in α+β titanium alloys, Mater. Sci. Eng. A 243(1) (1998) 206-211. https://doi.org/10.1016/s0921-5093(97)00802-2

[46] Q. Chao, P.D. Hodgson, H. Beladi, Thermal stability of an ultrafine grained Ti-6Al-4V alloy during post-deformation annealing, Mater. Sci. Eng. A 694 (2017) 13-23. https://doi.org/10.1016/j.msea.2017.03.082

[47] B. Wysocki, P. Maj, R. Sitek, J. Buhagiar, K.J. Kurzydlowski, W. Swieszkowski, Laser and Electron Beam Additive Manufacturing Methods of Fabricating Titanium Bone Implants, Appl. Sci. 7 (7) (2017) 657-677. https://doi.org/10.3390/app7070657

[48] Y. Zhai, H. Gallaraga, D.A. Lados, Microstructure static properties, and fatigue crack growth mechanisms in Ti-6Al-4V fabricated by additive manufacturing: LENS and EBM, Eng. Fail. Anal. 69 (2016) 3-14. https://doi.org/10.1016/j.engfailanal.2016.05.036

[49] G.M.T. Haar, T. Becker, Selective Laser Melting Produced Ti-6Al-4V: Post-Process Heat Treatments to Achieve Superior Tensile Properties, Materials. 11 (1) (2018) 146. https://doi.org/10.3390/ma11010146

[50] S. Spigarelli, C. Paoletti, M. Cabibbo, E. Cerri, E. Santecchia, On the creep performance of the Ti-6Al-4V alloy processed by additive manufacturing, Addit. Manuf. 49 (2022) 102520. https://doi.org/10.1016/j.addma.2021.102520

[51] W. Mei, Y. Wen, Martensitic transformation form β to α' and α'' phases in Ti-V alloys: A first-principles study, J. Mater. Res. 32 (2017) 3183-3190. https://doi.org/10.1557/jmr.2017.276

[52] F. Niessen, T. Nyyssoenen, A.A. Gadzer, R. Hielscher, Parent grain reconstruction from partially or fully transformed microstructure in MTEX. Mater. Sci. 2021. https://doi.org/10.48550/arXiv.2104.14603

[53] M. Neikter, A. Huang and X. Wu, Microstructural characterization of binary microstructure pattern in selective laser-melted Ti-6Al-4V, Int. G. Adv. Manuf. Technol. 104 (2019) 1381-1391. https://doi.org/10.1007/s00170-019-04002-58

[54] B. Baufeld, O. Biest, S. Dillien, Texture and Crystal Orientation in Ti-6Al-4V Build Fabricated by Shaped Metal Deposition, Metal. Mater. Trans. A 41(8) 2020) 1917-1927. https://doi.org/10.1007/s11661-010-0255-x

[55] Q. Zhang, J. Xie, T. London, D: Griffiths, I. Bhamji, V. Oancea, Estimates of the mechanical properties of laser powder bed fusion Ti-6Al-4V parts using finite element models, Mater. Des. 169 (2019) 107678. https://doi.org/10.1016/j.matdes.2019.107678
[56] M.P. Behera, T. Dougherty, S. Singamneni, K. De Silva, Selective laser melting of aluminium metal-matrix composites and the challenges, Mater. Today: Commun. 33 (8) (2020) 5729-5733. https://doi.org/10.1016/j.matpr.2020.05.086
[57] Q. Liu, J. Elambasseril, S. Sun, M. Leary, M. Brandt, P. Sharp, The Effect of Manufacturing Defects on the Fatigue Behaviour of Ti-6Al-4V Specimens Fabricated Using Selective Laser Melting, Adv. Mat. Res. 891-892 (2014) 1519-1524. https://doi.org/10.4028/www.scientific.net/AMR.891-892.1519
[58] H.G. Salem, L. Carter, M. Attallah, H.G. Salem, Influence of processing parameters on internal porosity and types of defects formed in Ti6Al4V lattice structure fabricated by selective laser melting, Mater. Sci. Eng. A 767 (2019) 138387. https://doi.org/10.1016/j.msea.2019.138387
[59] J. Vaithilingam, E. Prina, R.D. Goodridge, R.J.M. Hague, S. Edmondson, F.R.A.J. Rose, S.D.R. Christie, Surface chemistry of Ti6Al4V components fabricated using selective laser melting for biomedical applications. Mater. Sci. Eng. C. 67 (2016) 294-303. https://doi.org/10.1016/j.msec.2016.05.054
[60] S.C. Cox, P. Jamshidi, N.M. Eisenstein, M.A. Webber, H. Burton, R.J.A. Moakes, O. Addison, M.M. Attallah, D.E.T. Shepherd, L.M. Grover, Surface Finish has a Critical Influence on Biofilm Formation and Mammalian Cell Attachment to Additively Manufactured Prosthetics, ACS Biomater. Sci. Eng. 3 (8) (2017) 1616-1626. https://doi.org/10.1021/acsbiomaterials.7b00336
[61] J.-Y. Huang, C.-H. Chang, W.-C. Qang, M.-J., Chou, C.-C. Tseng, P.-W. Tu, Systematic evaluation of selective fusion additive manufacturing based on thermal energy source applied in processing of titanium alloy specimens for medical applications, Int. J., Adv. Manuf. Technol. 109 (2020) 2421-2429. https://doi.org/10.1007/s00170-020-05797-7
[62] S. Bagheron, J. Wehr, H.J. Maier, Application of mechanical surface finishing processes for roughness reduction and fatigue improvement of additively manufactured Ti-6Al-4V parts, Int. J. Farigue. 102 (2017) 135-142. https://doi.org/10.1016/j.ijfatigue.2017.05.008
[63] C.F. Hickey, Tensile Strength-Hardness Correlation for Titanium Alloys, ASTM, 1961, p. 26.
[64] J.S. Keist, T.A. Palmer, Development of strength-hardness relationships in additively manufactured titanium alloys, Mater. Sci. Eng. A 693 (2017) 214-224. https://doi.org/10.1016/j.msea.2017.03.012
[65] D. Barba, C. Alabort, Y.T. Tang, M.J. Viscasillas, R.C. Reed, E. Alabort, On the size and orientation effect in additive manufactured Ti-6Al-4V, Mater. Des. 186 (2020) 108235. https://doi.org/10.1016/j.matdes.2019.108235
[66] P. Ahmadian, S.M. Abbasi, M. Morakabati, The role of initial α-phase orientation on tensile and strain hardening behavior of Ti-6Al-4V alloy. Mater. Today Commun. 13 (2017) 332-345. https://doi.org/10.1016/j.mtcomm.2017.10.018
[67] G.B. Viswanathan, E. Lee, D.M. Maher, S. Banerjee, H.L. Fraser, Direct observations and analyses alpha phase of an alpha/beta Ti-alloy of dislocation substructures in the formed by

nanoindentation, Acta Mater. 53 (19) (2005) 5101-5115. https://doi.org/10.1016/j.actamat.2005.07.030
[68] C. Fizanne-Michel, M. Cornen, P. Castany, I. Peron, T. Gloriant, Determination of hardness and elastic modulus inverse pole figures of a polycrystalline commercially pure titanium by coupling nanoindentation and EBSD techniques, Mater. Sci. Eng. A. 613 (2014) 159-162. https://doi.org/10.1016/j.msea.2014.06.098
[69] D. Tabor, The hardness and strength metals, J. Met. 79(7) (1951) 1-18
[70] J. Cahoon, Improved equation relating hardness to ultimate strength, Metall. Trans. 3(11) (1972) 3040
[71] J. Cahoon, W.H. Broughto, A.R. Kutzak, Determination of yield strength from hardness measurements, Metall. Trans. 2(7) (1971) 1979-1983. https://doi.org/10.1007/BF02913433